Natural Resources for Human Health
eISSN: 2583-1194

Original Research

Received 10 May 2026
Revised 15 June 2026
Accepted 28 June 2026

Natural Resources for Human Health 2026, Vol. 6 (5): 1190–1214

KEYWORDS:
Green synthesis, silver nanoparticles, Bryophyllum pinnatum, Crassula ovata, DPPH, radical scavenging, MTT cytotoxicity, TNF-α, IL-6

Green Synthesis of Silver Nanoparticles using Crassula Ovata and Bryophyllum Pinnatum Leaf Extracts: Characterisation and Comparative Antioxidant, Cytotoxic and Anti-Inflammatory Activity of the Individual and Combined Systems

Somendra kumar[1], Tirthankar choudhury[2]

[1]Research scholar at School of Pharmacy, ITM University, Gwalior (M.P.)
[2]Prof. at School of Pharmacy, ITM University, Gwalior (M.P.)

ABSTRACT: Two members of the *Crassulaceae* with different secondary-metabolite profiles were used as reducing and capping systems for biogenic silver nanoparticles, and the resulting particles were carried through three unrelated *in vitro* endpoints under one protocol. Ethanolic leaf extracts of *Crassula ovata* and *Bryophyllum pinnatum* were reacted with 1 mM silver nitrate at a 1:9 extract-to-salt ratio (pH 8.0, 60 °C, 2 h, 24 h dark maturation) to give CO-AgNPs and BP-AgNPs. A 1:1 (w/w) physical mixture of the two purified powders (MIX-AgNPs) was carried as a combination arm. Both batches gave a single surface plasmon resonance band, at 422.77 ± 0.35 nm for CO-AgNPs and 427.20 ± 0.40 nm for BP-AgNPs, with no corresponding band in the solvent, salt or extract controls. Hydrodynamic diameter was 83.83 ± 1.25 nm and 75.57 ± 1.25 nm, polydispersity index 0.294 ± 0.011 and 0.252 ± 0.008, and zeta potential −28.37 ± 0.75 mV and −32.57 ± 0.80 mV. Diffraction peaks indexed to face-centred cubic silver, with mean crystallite sizes of 29.75 ± 3.70 nm and 23.87 ± 2.29 nm; energy-dispersive X-ray analysis returned 67.15 wt% and 70.18 wt% silver with carbon and oxygen signals consistent with an adsorbed phytochemical layer. Cumulative silver-equivalent release over 24 h in phosphate-buffered saline pH 7.4 reached 84.10 ± 2.55% and 88.60 ± 2.60%. The potency order was the same on every endpoint: MIX-AgNPs > BP-AgNPs > CO-AgNPs > BP-EXT > CO-EXT. DPPH IC50 fell from 106.13 µg/mL for the *C. ovata* extract to 34.79 µg/mL for MIX-AgNPs, against 10.60 µg/mL for ascorbic acid. At 24 h the MTT IC50 for MIX-AgNPs was 65.68 µg/mL (MCF-7), 76.60 µg/mL (HCT116) and 89.00 µg/mL (A549), three- to six-fold below the parent extracts. In lipopolysaccharide-stimulated RAW 264.7 macrophages held at or above 80% viability, MIX-AgNPs lowered TNF-α by 75.07 ± 2.06% and IL-6 by 75.05 ± 2.33% at 50 µg/mL. After Holm adjustment the mixture was not consistently better than BP-AgNPs at matched concentrations, so the combination result is reported as enhanced activity and not as synergy.

1. INTRODUCTION

The *Crassulaceae* contain roughly 1,400 succulent species, and two of them, *Crassula ovata* (Mill.) Druce and *Bryophyllum pinnatum* (Lam.) Oken, carry long ethnobotanical records for wound care, inflammatory complaints and infection. Their chemistry is not the same. *B. pinnatum* is defined by bufadienolide cardiac glycosides together with quercetin- and kaempferol-type flavonol glycosides, a profile mapped in detail by metabolite profiling and quantified by UHPLC-MS/MS (Fürer et al., 2013; Oufir et

al., 2015; Fürer et al., 2016). *C. ovata* is dominated by flavonoid aglycones and pentacyclic triterpenoids. Both species share the crassulacean acid metabolism route, which leaves the leaf tissue loaded with organic acids and the calcium, potassium and magnesium salts that neutralise them (Gilman & Edwards, 2020). Controlled pharmacology on *B. pinnatum* has kept those two chemistries apart. The flavonoid fraction carries most of the inhibition of porcine detrusor contractility (Fürer et al., 2015; Bachmann et al., 2017), the bufadienolide fraction is the stronger inhibitor of human myometrial contraction and of oxytocin-driven calcium and MAPK signalling (Santos et al., 2019; Santos et al., 2021), and a cream formulated with the major leaf flavonoid matches the whole aqueous extract in a rat excision wound model (Coutinho et al., 2021). An extract taken whole therefore carries both classes into the reaction flask.

That difference matters for nanoparticle work. Reduction of Ag^{+} to Ag^{0} by a plant extract is driven by the phenolic and carbonyl-bearing fraction, and the same molecules stay adsorbed on the growing surface and set the final size, charge and dispersion state (Sharma et al., 2009; Patil & Kim, 2017; Huq et al., 2022; Thomas et al., 2024). Two extracts with different phenolic pools should therefore give two different particle populations from an identical reaction, and any biological difference downstream can be traced back to the extract rather than to the process.

Most published green-synthesis work uses a single species and a single endpoint. Comparative designs in which two chemically distinct extracts are pushed through the same reaction, purified the same way and then tested on the same panel are much less common, and without them it is difficult to separate a genuine plant effect from batch-to-batch variation in synthesis conditions. Reports on *Kalanchoe pinnata*, the accepted synonym of *B. pinnatum*, show selective cytotoxicity in cancer cell lines through ROS-mediated apoptosis and describe the extract as a candidate adjuvant (Hernández-Caballero et al., 2022; Faundes-Gandolfo et al., 2024), but the nanoparticle form of the same extract has not been placed alongside a related species under matched conditions.

A third arm was added for a specific reason. Combination behaviour in nanoparticle systems is usually inferred from a lower mean or a lower fitted IC50, which is not evidence of interaction (Chou, 2010). A 1:1 physical mixture of two independently synthesised and purified colloids separates a combination effect from a co-reduction product, because the two particle populations are formed apart and only meet in the assay well. Silver nanoparticles combined with a cytotoxic drug can produce a formally synergistic combination index (Rivera et al., 2024), so the question is worth posing, provided the claim is kept inside what the design can support.

The work reported here had four aims: to synthesise silver nanoparticles from ethanolic leaf extracts of *C. ovata* and *B. pinnatum* under one fixed protocol; to characterise both batches by UV-visible spectroscopy, dynamic and electrophoretic light scattering, X-ray diffraction, transmission electron microscopy, infrared spectroscopy and EDX, and to quantify silver-equivalent content and release; to compare the two nanoparticle systems, their parent extracts and a 1:1 physical mixture on radical scavenging, cytotoxicity against three human cancer cell lines and cytokine suppression in stimulated macrophages; and to state the interaction result at the level the design allows.

2. MATERIALS AND METHODS

2.1 Chemicals and reagents

Silver nitrate, sodium hydroxide, absolute ethanol, methanol (HPLC grade), 2,2-diphenyl-1-picrylhydrazyl (DPPH), ascorbic acid, 3-(4,5-dimethylthiazol-2-yl)-2,5-diphenyltetrazolium bromide (MTT), dimethyl sulfoxide (DMSO), Dulbecco's modified Eagle medium (high glucose), foetal bovine serum, penicillin-streptomycin, lipopolysaccharide from *Escherichia coli* and dexamethasone were of analytical or cell-culture grade. Mouse TNF-α and IL-6 sandwich ELISA kits were used as supplied. Deionised water was used throughout.

2.2 Plant material, authentication and raw-material quality control

Fresh mature leaves of *C. ovata* and *B. pinnatum* were collected in February 2025 from a botanic Eco-museum Tapovan (Nursery of Forest Department) and Italian garden phoolbag Gwalior Madhya Pradesh, India (altitude 197 m). Leaves were washed in potable water, shade-dried at 25 ± 5 °C for 15 days to a residual moisture below 12%, milled and passed through a #40 sieve (425 µm), then stored in the dark in closed containers. Voucher specimens were deposited to Botanical survey of india ,Central National Herbarium Howrah that Ref. No. CNH/Tech.II/2026/21 and Specimen Numbers ITM/SK-01 (*C. ovata*) and ITM/SK-02 (*B. pinnatum*).

Physicochemical constants of both powders were determined in triplicate following Indian Pharmacopoeia 2022 appendices 2.2.32, 2.3.19 and 2.4.16 (Indian Pharmacopoeia Commission, 2022): loss on drying at 105 ± 2 °C to constant weight; total ash by incineration at 450 ± 25 °C; acid-insoluble ash by boiling the total ash with 25 mL of 2 M hydrochloric acid for 10 min; water-soluble ash by boiling the total ash with 25 mL of water for 5 min; and swelling index on 1.000 g of powder moistened with 1 mL ethanol and made to 25 mL with water. Results are given in Table 1 and were used only as an identity and cleanliness check on the starting material.

2.3 Extraction

Powdered leaf (1:10 w/v) was macerated in 70% (v/v) ethanol for 72 h at room temperature with intermittent shaking, filtered through Whatman No. 1 paper and concentrated on a rotary evaporator at 40 °C to a dry residue. The 70% ethanol system was selected because it gave a higher extractive value than 95% ethanol for both species (15.17 ± 0.35% and 17.90 ± 0.30% w/w for *C. ovata* and *B. pinnatum* respectively, against 10.03 ± 0.25% and 11.43 ± 0.31% w/w in 95% ethanol). Dried extracts are referred to below as CO-EXT and BP-EXT.

2.4 Extract working solution

For each synthesis, 100 mg of dried extract was dispersed in 10 mL of deionised water to give a 10 mg/mL working solution, sonicated for 10 min, centrifuged at 5,000 rpm for 10 min and filtered through a 0.45 µm membrane. The clear filtrate was used immediately. This step removes coarse plant residue that would otherwise seed uncontrolled nucleation while leaving the soluble reducing and capping fraction in solution.

2.5 Synthesis of silver nanoparticles

Silver nitrate solution (1 mM) was prepared fresh by dissolving 16.99 mg in deionised water and making up to 100 mL. For each batch, 90 mL of this solution was transferred to a 250 mL conical flask, heated to 60 °C on a magnetic stirrer, and 10 mL of the 10 mg/mL extract working solution was added dropwise under continuous stirring, fixing the extract-to-salt ratio at 1:9 and the final volume at 100 mL. The reaction pH was adjusted to 8.0 with 0.1 N sodium hydroxide. Alkaline pH deprotonates phenolic hydroxyls and raises the electron-donating capacity of the extract towards Ag^{+}. The mixture was stirred at 500 rpm for 2 h at 60 °C in a foil-wrapped flask to exclude photoreduction, then left undisturbed in the dark at room temperature for 24 h. The two batches are designated CO-AgNPs and BP-AgNPs.

2.6 Purification and drying

Each suspension was centrifuged at 12,000 rpm for 20 min, the supernatant discarded and the pellet washed three times with deionised water to remove unreacted silver ions and loosely associated organics. After the final wash the pellet was redispersed in 10 mL of deionised water. A portion was dried at 40 °C to constant weight and stored in amber airtight vials at room temperature.

2.7 Preparation of the combination arm

MIX-AgNPs was prepared immediately before each assay by weighing equal masses of dried CO-AgNPs and BP-AgNPs and dispersing them together in the assay vehicle. Concentrations quoted for MIX-AgNPs are total nanoparticle concentrations: 100 µg/mL contains 50 µg/mL of each component. No co-reduction or co-milling step was used.

2.8 UV-visible spectroscopy

Purified suspensions were diluted 1:10 with deionised water and scanned from 300 to 800 nm at 1 nm intervals in a 1 cm quartz cell against a deionised water blank (n = 3). Deionised water, 1 mM silver nitrate and each extract were scanned as controls. Full width at half maximum was read from the mean spectrum, and the ratio of absorbance at 650 nm to peak absorbance (A650/Amax) was calculated as an aggregation indicator.

2.9 Calibration and silver-equivalent content

Dried nanoparticles were dispersed in deionised water and diluted to 5, 10, 20, 30, 40 and 50 µg/mL. Absorbance was recorded at 425 nm in triplicate. Limit of detection and limit of quantitation were calculated as $3.3\sigma/S$ and $10\sigma/S$, where σ is the residual standard deviation of the regression and S the slope. For content determination, weighed dried nanoparticles were dispersed

and diluted to a theoretical 25 μg/mL; measured concentration was obtained from the regression equation and expressed as a percentage of theoretical.

2.10 Particle size, polydispersity and zeta potential

Hydrodynamic diameter and polydispersity index were measured by dynamic light scattering and zeta potential by electrophoretic light scattering, on diluted aqueous dispersions at 25 °C in triplicate (disposable sizing cuvette; clear disposable zeta cell, 12 zeta runs).

2.11 X-ray diffraction

Diffractograms were recorded over 2θ = 20-80° with Cu Kα radiation (λ = 1.5406 Å). Peaks were indexed against the face-centred cubic silver lattice and crystallite size was calculated from the Debye-Scherrer relation using the full width at half maximum of each indexed reflection.

2.12 Transmission electron microscopy

Purified dispersion was diluted, sonicated for 2 min and drop-cast on a carbon-coated copper grid, wicked after 60 s and air-dried. Imaging was performed on a Hitachi HC-1 at 120 kV at ×40k with a 200 nm scale bar. Particle diameters were measured from two non-overlapping fields per batch. Aspect ratio and circularity were computed from the same micrographs; both are dimensionless and required no length calibration.

2.13 Infrared spectroscopy

Spectra were recorded on a Bruker instrument with a diamond attenuated total reflectance accessory over 4000-400 cm^{-1}. Each nanoparticle batch was run against its own parent extract in the same session, since the measurement is the difference between the pair. Band positions were taken from the instrument peak-pick.

2.14 EDX

Dried nanoparticles were mounted on carbon conductive tape and analysed at 15 kV on a JED-2300 analysis station, with quantitation by the ZAF standardless method. Spectra are reported as elemental confirmation; quantitative metal content is given by the UV calibration in Table 4.

2.15 In vitro release

Release was followed by the dialysis membrane method. Nanoparticle equivalent to 2 mg was dispersed in 2 mL of medium inside a 12-14 kDa cut-off membrane and immersed in 50 mL of phosphate-buffered saline pH 7.4 at 37 ± 0.5 °C with stirring at 100 rpm. Samples of 2 mL were withdrawn at 0.5, 1, 2, 4, 6, 8, 12 and 24 h and replaced with fresh medium. Silver-equivalent concentration was read at 425 nm against the calibration equation. Cumulative amount was corrected for withdrawal as $Q_n = C_n V_r + \Sigma C_i V_s$, where Cn is the concentration at time n, Vr the receptor volume, Ci the concentrations of earlier samples and Vs the sampling volume. Cumulative release was expressed against the measured silver-equivalent content of the weighed sample rather than its nominal mass.

2.16 DPPH radical scavenging

Test materials were assayed at 6.25, 12.5, 25, 50, 75, 100, 150 and 200 μg/mL against 0.1 mM DPPH in methanol with 30 min incubation in the dark and reading at 517 nm (n = 3). Ascorbic acid (2.5-80 μg/mL) was the reference antioxidant. Because both extracts and metallic colloids absorb and scatter at 517 nm, every concentration was run with a matched sample blank containing the test material without DPPH, and corrected absorbance was taken as reaction absorbance minus sample blank absorbance. Scavenging was calculated as (DPPH control absorbance − corrected sample absorbance) / DPPH control absorbance × 100.

2.17 MTT cytotoxicity

MCF-7 breast, HCT116 colorectal and A549 lung carcinoma cells were maintained in high-glucose DMEM with 10% foetal bovine serum and 1% penicillin-streptomycin at 37 °C in a humidified 5% CO_2 atmosphere. Cryovials were thawed at 37 °C, diluted, centrifuged at 1,000 rpm for 5 min, seeded into T-25 flasks, allowed 24 h to attach and passaged at least once before assay. Cells were seeded at 1×10^4 per well in 100 μL in flat-bottom 96-well plates and left 24 h to attach, then exposed for 24

h to 6.25-800 µg/mL of each test material. Vehicle DMSO was held at or below 0.5% v/v. MTT (0.5 mg/mL in PBS, 20 µL per well) was added for 4 h at 37 °C in the dark, the medium removed and formazan dissolved in 100 µL DMSO before reading at 570 nm (Mosmann, 1983). Because plant extracts and metallic nanoparticles interfere with tetrazolium assays (Holder et al., 2012; Tournebize et al., 2013), each concentration of each test material was run as a cell-free blank in complete assay matrix and carried through the identical MTT, solubilisation and reading sequence; corrected absorbance is raw absorbance minus the matched blank. Viability was expressed against the matched corrected untreated control, and cytotoxicity as 100 minus viability, following the reduction-of-viability convention on which the ISO 10993-5 cytotoxicity categories rest (International Organization for Standardization, 2009). Replicates were technical, n = 3, rows A-C.

Viability values slightly above 100% were retained rather than clipped, so that assay variability is visible in the primary endpoint. In the derived cytotoxicity column only, negative values were reported as 0.00% and flagged.

2.18 Anti-inflammatory evaluation

RAW 264.7 murine macrophages were pre-treated for 2 h with test material at 3.125, 6.25, 12.5, 25 and 50 µg/mL and then challenged with lipopolysaccharide at 100 ng/mL for 24 h. Dexamethasone at 1 µM was the reference anti-inflammatory. Clarified supernatants were diluted 1:2 and assayed for TNF-α and IL-6 by sandwich ELISA (OD450 corrected at 570 nm). Standard curves were fitted with a four-parameter logistic model and sample concentrations obtained by inverse interpolation, then multiplied by the dilution factor. Cytokine inhibition was calculated as (LPS mean − treatment value) / (LPS mean − unstimulated mean) × 100. A parallel MTT viability plate with material-matched optical blanks was run under identical treatment conditions, and 80% viability was set in advance as the threshold below which cytokine suppression would not be interpreted as an anti-inflammatory effect.

2.19 Statistical analysis

Results are mean ± standard deviation of three replicates. Concentration-response data were fitted with a normalised variable-slope logistic model to individual replicate observations rather than to concentration means, and IC50 values are reported with 95% confidence intervals, Hill slope and the coefficient of determination computed across all replicate points. Treatment and concentration effects were tested by two-way analysis of variance recomputed from replicate-level values on a balanced design. Silver-equivalent content of the two batches was compared by an unpaired t-test on the replicate values; release profiles by two-way ANOVA with Šídák's multiple comparison test; and cytokine data by two-way ANOVA followed by Welch tests with Holm adjustment against the LPS control. Significance codes are ns for $p > 0.05$, * for $p < 0.05$, ** for $p < 0.01$, *** for $p < 0.001$ and **** for $p < 0.0001$. Curve quality was judged from the observations and was not adjusted towards a target R^2; analytical calibration curves and biological concentration-response curves are interpreted against different expectations, since the two have different sources of variance.

3. RESULTS AND DISCUSSION

3.1 Raw-material quality control

Loss on drying was 9.18 ± 0.22% for *C. ovata* and 10.98 ± 0.27% for *B. pinnatum*, both inside the 8-12% band expected for dried leaf powders. Acid-insoluble ash was 1.28 ± 0.07% and 1.55 ± 0.07%, comfortably under the 2.0% pharmacopoeial ceiling, which rules out meaningful contamination with sand or extraneous earth. Total ash was high in both species, 16.66 ± 0.24% and 18.86 ± 0.28%, above the 10-12% typical of leafy crude drugs. That excess is a property of the tissue rather than a cleanliness failure: crassulacean acid metabolism plants accumulate calcium, potassium and magnesium to buffer the organic acids stored overnight in leaf vacuoles (Gilman & Edwards, 2020), and calcium oxalate decomposes to calcium oxide on ignition. The low acid-insoluble ash beside the high total ash separates the two explanations. Swelling index was 5.17 ± 0.29 mL/g and 7.33 ± 0.29 mL/g and tracked loss on drying in the same direction, both reflecting the larger hydrophilic mucilage fraction of *B. pinnatum* (Table 1).

Table 1. Physicochemical constants of the dried leaf powders (mean ± SD, n = 3)

Parameter	*Crassula ovata*	*Bryophyllum pinnatum*	Pharmacopoeial reference
Loss on drying (% w/w)	9.18 ± 0.22	10.98 ± 0.27	NMT 12-14% (leafy drugs)
Total ash (% w/w)	16.66 ± 0.24	18.86 ± 0.28	NMT 16%
Acid-insoluble ash (% w/w)	1.28 ± 0.07	1.55 ± 0.07	NMT 2.0%
Water-soluble ash (% w/w)	7.98 ± 0.11	9.17 ± 0.18	NLT 5%
Swelling index (mL/g)	5.17 ± 0.29	7.33 ± 0.29	Report value
Extractive value, 70% ethanol (% w/w)	15.17 ± 0.35	17.90 ± 0.30	Report value
Extractive value, 95% ethanol (% w/w)	10.03 ± 0.25	11.43 ± 0.31	Report value

NMT, not more than; NLT, not less than. Total ash above the 10-12% typical of leafy crude drugs is a chemotaxonomic feature of crassulacean acid metabolism species rather than a contamination artefact; the low acid-insoluble ash discriminates between the two explanations.

3.2 Synthesis and yield

Colour change was visible within minutes of extract addition in both reactions. CO-AgNPs moved from pale yellow through yellowish brown to brown with onset at 7 min; BP-AgNPs darkened faster, with onset at 5 min and a final dark brown. No precipitation was seen in either flask during the reaction or over the 24 h maturation period. Reaction pH drifted down slightly from the 8.0 set point, to 7.72 for CO-AgNPs and 7.68 for BP-AgNPs, consistent with proton release during phenolic oxidation. Dry yield after purification was 17.83 ± 0.22 mg per 100 mL for CO-AgNPs and 19.40 ± 0.27 mg per 100 mL for BP-AgNPs. Both pellets redispersed in water, CO-AgNPs freely and BP-AgNPs after brief vortexing, and supernatants were close to colourless by the third wash.

Table 2. Synthesis conditions, visual observations and dry yield

Parameter	CO-AgNPs	BP-AgNPs
Extract	*C. ovata* ethanolic	*B. pinnatum* ethanolic
Metal salt / concentration	$AgNO_3$, 1 mM	$AgNO_3$, 1 mM
Extract-to-salt ratio (v/v)	1:9	1:9
Extract concentration / volume	10 mg/mL, 10 mL	10 mg/mL, 10 mL
Final reaction volume	100 mL	100 mL
Set pH / pH after reaction	8.0 / 7.72	8.0 / 7.68
Temperature / stirring / time	60 °C, 500 rpm, 2 h	60 °C, 500 rpm, 2 h
Maturation	24 h, dark, room temperature	24 h, dark, room temperature
Onset of colour change	7 min	5 min
Colour after maturation	Brown	Dark brown
Visible precipitation	Not observed	Not observed
Purification	12,000 rpm, 20 min; 3 washes	12,000 rpm, 20 min; 3 washes
Redispersion behaviour	Freely redispersed	Redispersed after mild vortexing
Dry yield (mg/100 mL)	17.83 ± 0.22	19.40 ± 0.27

Natural Resources for Human Health
eISSN: 2583-1194

3.3 UV-visible spectra

Each purified suspension gave one symmetric surface plasmon resonance band and no secondary feature. Peak position was 422.77 ± 0.35 nm for CO-AgNPs and 427.20 ± 0.40 nm for BP-AgNPs, both inside the 400-450 nm window characteristic of colloidal silver. Peak absorbance was 0.844 ± 0.006 and 0.911 ± 0.007, with coefficients of variation below 1.0% across replicates. Band width differed: 74.47 ± 0.65 nm for CO-AgNPs against 78.90 ± 0.66 nm for BP-AgNPs. The A650/Amax ratio was 0.123 and 0.141 respectively, low enough in both cases to exclude substantial aggregation. Deionised water, 1 mM silver nitrate and both extract blanks gave no band in the plasmon region; extract absorbance was confined below 380 nm (Table 3, Fig. 1a-b).

Table 3. UV-visible spectral parameters of the purified nanoparticle suspensions (mean ± SD, n = 3)

Batch	λmax (nm)	Amax	CV of Amax (%)	FWHM (nm)	A650	A650/Amax	Band profile
CO-AgNPs	422.77 ± 0.35	0.844 ± 0.006	0.65	74.47 ± 0.65	0.104	0.123	Single SPR band
BP-AgNPs	427.20 ± 0.40	0.911 ± 0.007	0.77	78.90 ± 0.66	0.128	0.141	Single SPR band

Controls: deionised water, 1 mM silver nitrate and both ethanolic extract blanks gave no band between 400 and 450 nm; extract absorbance was confined below 380 nm.

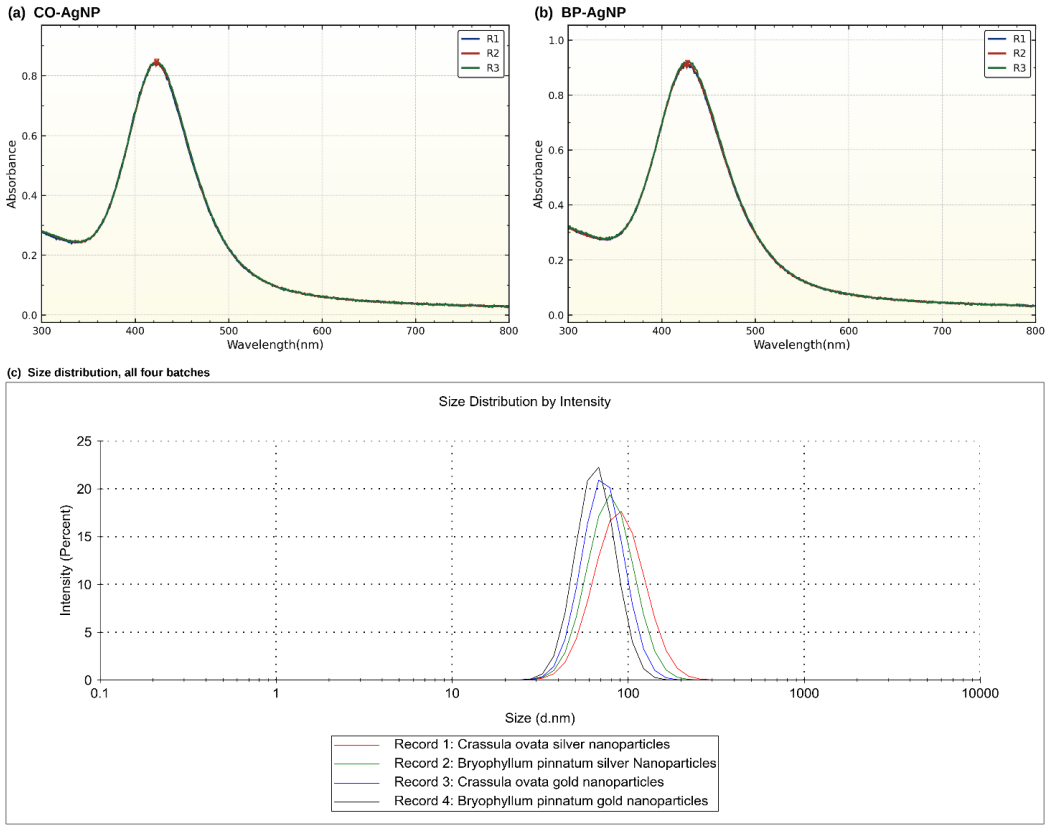

Figure 1. Optical and colloidal characterisation. UV-visible absorption spectra of the purified suspensions, 300-800 nm at 1 nm interval, three scans overlaid: (a) CO-AgNPs, mean peak 422.77 nm; (b) BP-AgNPs, mean peak 427.20 nm. (c) Intensity-weighted size distribution by dynamic light scattering in water at 25 °C; records 1 and 2 are the silver batches reported here, records 3 and 4 the gold batches from the same two extracts in the companion study, shown for reference only. A single plasmon band is present in each spectrum and all distributions are monomodal. No band was recorded in the deionised water, silver nitrate or extract controls.

3.4 Calibration and silver-equivalent content

Absorbance at 425 nm was linear from 5 to 50 μg/mL, giving y = 0.01795x + 0.00533 with R^2 = 0.9998 and residual standard deviation 0.00528, from which the limit of detection was 0.97 μg/mL and the limit of quantitation 2.94 μg/mL. Back-calculated accuracy ranged from 96.81% to 104.49% across the six levels and residuals showed no trend with concentration. Measured silver-equivalent content of the dried batches was 96.85 ± 1.12% for CO-AgNPs and 99.35 ± 0.80% for BP-AgNPs, with relative standard deviations of 1.16% and 0.81%. Recomputed from the replicate values, the 2.49-percentage-point gap between the two batches was statistically detectable (unpaired t-test, t(4) = 3.14, p = 0.035), but both sit inside the 95-105% window normally accepted for content uniformity, and the difference is an order of magnitude smaller than the fold changes measured in the biological assays (Table 4).

Table 4. Calibration performance at 425 nm and silver-equivalent content of the dried batches

Parameter	Value
Concentration range	5-50 μg/mL
Regression equation	y = 0.01795x + 0.00533
Coefficient of determination	0.9998 (exact 0.99977)
Residual standard deviation, Sy/x	0.00528
Limit of detection	0.97 μg/mL
Limit of quantitation	2.94 μg/mL
Back-calculated accuracy across six levels	96.81-104.49%
CO-AgNPs content (theoretical 25 μg/mL)	96.85 ± 1.12% (RSD 1.16%)
BP-AgNPs content (theoretical 25 μg/mL)	99.35 ± 0.80% (RSD 0.81%)
CO-AgNPs versus BP-AgNPs content	t(4) = 3.14, p = 0.035 (unpaired t-test on replicates)
Content uniformity window	Both batches within 95-105% of theoretical

3.5 Particle size, polydispersity and zeta potential

BP-AgNPs was the smaller and the more highly charged of the two. Hydrodynamic diameter was 75.57 ± 1.25 nm against 83.83 ± 1.25 nm for CO-AgNPs, polydispersity index 0.252 ± 0.008 against 0.294 ± 0.011, and zeta potential −32.57 ± 0.80 mV against −28.37 ± 0.75 mV. Intensity distributions were monomodal for both batches, with a single peak accounting for 100% of intensity and distribution widths of 25.6 nm and 31.8 nm. Both zeta values sit in the range normally taken to indicate electrostatically stabilised colloids, and the more negative value for BP-AgNPs matches its narrower size distribution (Table 5, Fig. 1c).

Table 5. Particle size, polydispersity index and zeta potential (mean ± SD, n = 3, 25 °C)

Batch	Hydrodynamic diameter (nm)	Polydispersity index	Zeta potential (mV)	Distribution width (nm)
CO-AgNPs	83.83 ± 1.25	0.294 ± 0.011	−28.37 ± 0.75	31.8
BP-AgNPs	75.57 ± 1.25	0.252 ± 0.008	−32.57 ± 0.80	25.6

Both batches gave monomodal intensity distributions with a single peak accounting for 100% of scattered intensity.

3.6 X-ray diffraction

Both samples gave four reflections indexing to the face-centred cubic silver lattice. CO-AgNPs peaked at 38.12°, 44.31°, 64.43° and 77.39°, assigned to (111), (200), (220) and (311), with a mean crystallite size of 29.75 ± 3.70 nm. BP-AgNPs peaked at 38.20°, 44.42°, 64.58° and 77.52° with broader lines and a mean crystallite size of 23.87 ± 2.29 nm. The (111) reflection was the most intense in both, and relative intensities fell in the same order across the remaining planes. Low-intensity broad background was present between 20° and 35°, more so in BP-AgNPs; these features were not indexed to metallic planes and are attributed to the amorphous organic capping layer (Table 6, Fig. 2a-b).

Table 6. X-ray diffraction parameters (Cu Kα, λ = 1.5406 Å)

Batch	2θ (°)	hkl	Relative intensity (%)	FWHM (°)	d-spacing (Å)	Crystallite size (nm)
CO-AgNPs	38.12	(111)	100	0.24	2.359	35.02
CO-AgNPs	44.31	(200)	52	0.29	2.043	29.58
CO-AgNPs	64.43	(220)	29	0.34	1.445	27.62
CO-AgNPs	77.39	(311)	21	0.38	1.232	26.79
BP-AgNPs	38.20	(111)	100	0.31	2.354	27.12
BP-AgNPs	44.42	(200)	50	0.36	2.038	23.84
BP-AgNPs	64.58	(220)	27	0.42	1.442	22.38
BP-AgNPs	77.52	(311)	20	0.46	1.230	22.15

Mean crystallite size: CO-AgNP 29.75 ± 3.70 nm; BP-AgNP 23.87 ± 2.29 nm. Broad unindexed background between 20° and 35°, stronger in BP-AgNP, is attributed to the amorphous organic capping layer.

3.7 Transmission electron microscopy

Counted micrographs placed the metal core well below the hydrodynamic diameter, as expected, and above the crystallite size, as required. The number-mean core diameter was 32.04 ± 15.64 nm for CO-AgNPs across 125 particles and 29.54 ± 14.05 nm for BP-AgNPs across 125 particles, with geometric standard deviations of 1.657 and 1.607 and D90 values of 50.85 and 48.15 nm. The ratio of Z-average to counted mean was 2.62 and 2.56. Both means exceed the corresponding Debye-Scherrer crystallite size, giving 1.25 and 1.89 coherent domains per particle on a cubed diameter basis, so CO-AgNPs is close to single-crystalline and BP-AgNPs marginally polycrystalline. Shape descriptors were computed without a length calibration, since aspect ratio and circularity are dimensionless: 6.4% of CO-AgNPs and 5.6% of BP-AgNPs particles exceeded an aspect ratio of 2.0, with median aspect ratios of 1.25 and 1.20 and median circularities of 0.83 and 0.85. Both populations are therefore quasi-spherical to polyhedral, and the anisotropic fraction is small enough to be consistent with the single symmetric plasmon band and the low A650/Amax ratios recorded in Table 3 (Table 7, Fig. 3).

Table 7. Transmission electron microscopy: counted particle size and shape census

Parameter	CO-AgNPs	BP-AgNPs
Particles counted	125	125
Number-mean core diameter (nm)	32.04 ± 15.64	29.54 ± 14.05
D10 / D50 / D90 (nm)	13.57 / 29.38 / 50.85	13.55 / 27.06 / 48.15
Geometric standard deviation	1.657	1.607
Debye-Scherrer crystallite size (nm)	29.75 ± 3.70	23.87 ± 2.29

Parameter	CO-AgNPs	BP-AgNPs
Ratio, DLS Z-average : TEM mean	2.62	2.56
Aspect ratio > 2.0 (% of particles)	6.4	5.6
Median aspect ratio	1.25	1.20
Median circularity	0.83	0.85

Counted from two non-overlapping fields per batch at ×40k. Shape descriptors are dimensionless and were computed from the micrographs without a length calibration. The mean core diameter exceeds the crystallite size in both batches, as it must, and the ratio of hydrodynamic to core diameter is consistent with an adsorbed capping and hydration layer that light scattering sees and electron microscopy does not.

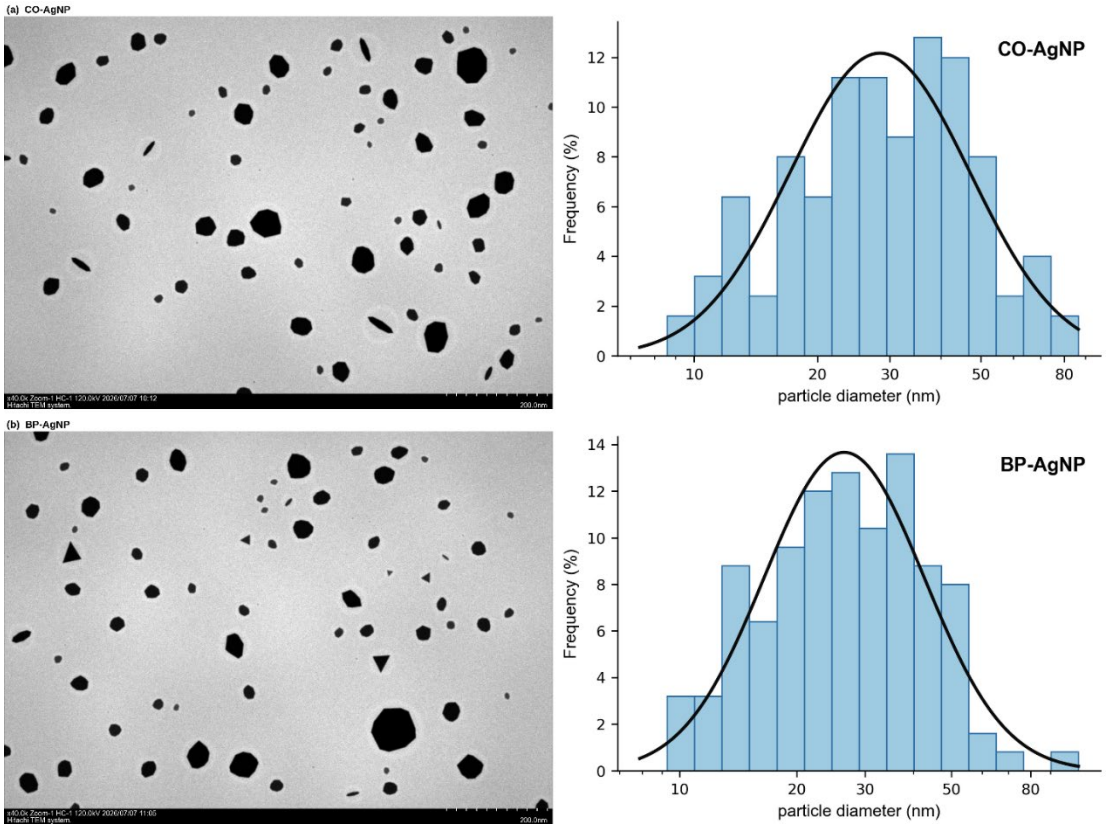

Figure 3. Transmission electron micrographs and number-weighted size distributions: (a) CO-AgNPs and (b) BP-AgNPs (Hitachi HC-1, 120 kV, ×40k; scale bar 200 nm). Histograms are the counted particle diameters with a lognormal fit overlaid.

3.8 Infrared spectroscopy of the capping layer

The parent extract and its nanoparticle were run as a matched pair for each species, since the reading is the difference between them. Aliphatic C-H stretching moved by no more than 6 cm^{-1} in either system, which fixes the internal reference and validates the shifts measured elsewhere in the spectrum. Against that reference, the hydroxyl stretch of BP-EXT moved from 3478 to 3434 cm^{-1} on nanoparticle formation and the second hydroxyl feature from 3284 to 3244 cm^{-1}, the carbonyl from 1738 to 1724 cm^{-1}, and the glycosidic C-O-C envelope from 1036 to 1020 cm^{-1}, all to lower wavenumber and all consistent with coordination of oxygenated groups to the metal surface.

Two bands appear in the nanoparticle spectra that are not present in either extract: an asymmetric carboxylate stretch at 1588 cm^{-1} for CO-AgNPs and 1586 cm^{-1} for BP-AgNPs, paired with a symmetric stretch at 1396 and 1394 cm^{-1}. The separation

between them is 192 cm^{-1} in both batches, which falls in the bridging bidentate range and identifies the binding geometry rather than merely confirming that a capping layer is present. Neither spectrum carries a sharp isolated band at 1384 cm^{-1}, so the symmetric carboxylate assignment is not confounded by nitrate carried over from the precursor. One further difference separates the two species: the carbonyl band is no longer resolved in CO-AgNPs, whereas BP-AgNPs retains it at 1724 cm^{-1}, indicating that the carbonyl-bearing fraction of the *C. ovata* extract is more completely consumed during reduction (Table 8, Figs. 4 and 5).

Table 8. ATR-FTIR band positions and shifts on nanoparticle formation (cm^{-1})

Band	BP-EXT	BP-AgNPs	Δν	CO-AgNPs	Role
ν(O-H)	3478	3434	−44	3438	Coordination
ν(O-H)	3284	3244	−40	3250	Coordination
ν_as(C-H)	2924	2918	−6	2918	Reference
ν_s(C-H)	2854	2850	−4	2848	Reference
ν(C=O)	1738	1724	−14	not resolved	Coordination
ν_as(COO^-)	absent	1586	new band	1588	Diagnostic
ν_s(COO^-)	absent	1394	new band	1396	Diagnostic
δ(C-H)	1462	1458	−4	1458	—
ν(C-O-C)	1036	1020	−16	1022	Coordination

Diamond ATR, 4000-400 cm^{-1}; positions are peak-picked from the instrument output. Shifts are tabulated for the *B. pinnatum* pair, for which both members carry a peak-picked list. CO-AgNP positions are given as absolute values against the *C. ovata* extract spectrum in Figure 4; the peak-picked list for that extract is outstanding, so the corresponding shift column is not tabulated. Carboxylate separation Δν(as-sym) is 192 cm^{-1} for both silver batches, in the bridging bidentate range of 140-210 cm^{-1}. Neither spectrum carries a sharp isolated band at 1384 cm^{-1}, so residual nitrate from the precursor is excluded.

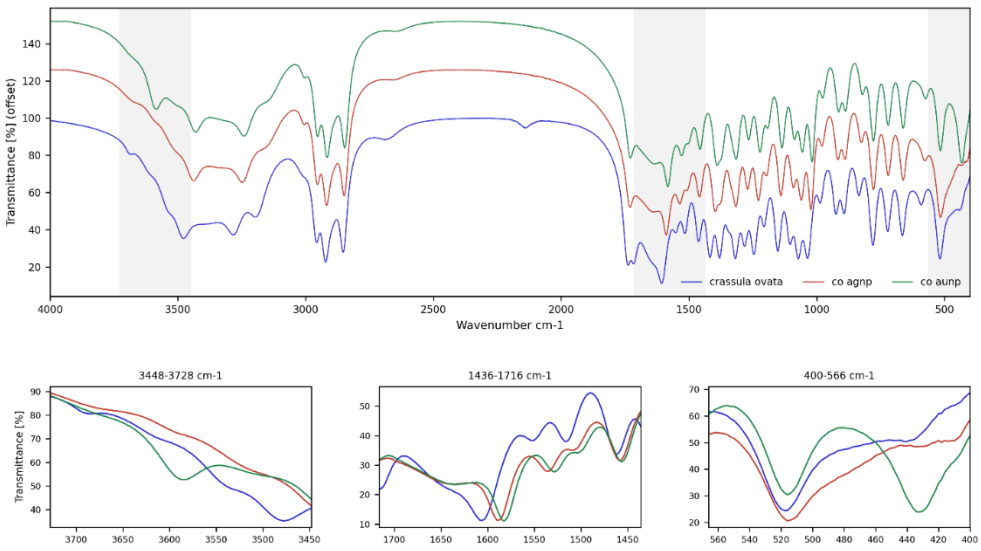

Figure 4. ATR-FTIR spectra of the *Crassula ovata* system, 4000-400 cm^{-1}, offset for clarity, with three regions expanded below. The extract trace is the reference against which the nanoparticle shifts in Table 8 are measured. The trace for the gold batch prepared from the same extract is included for reference only and is reported in the companion study.

Natural Resources for Human Health
eISSN: 2583-1194

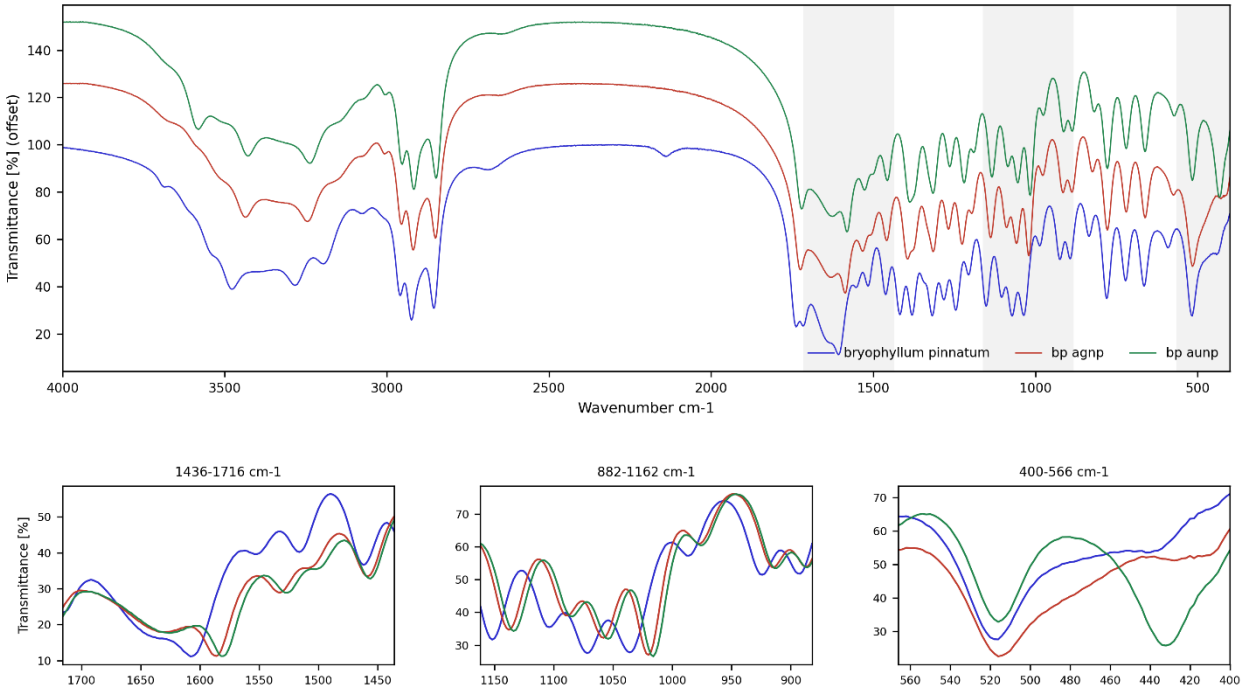

Figure 5. ATR-FTIR spectra of the *Bryophyllum pinnatum* system, 4000-400 cm^{-1}, offset for clarity, with three regions expanded below. The trace for the gold batch prepared from the same extract is included for reference only.

3.9 Elemental composition

Energy-dispersive X-ray analysis put silver as the dominant element by mass in both batches: 67.15 wt% (21.79 at%) for CO-AgNPs and 70.18 wt% (24.45 at%) for BP-AgNPs, in each case from an intense Ag Lα line near 2.98 keV. Carbon and oxygen accounted for 12.41 and 18.29 wt% in CO-AgNPs and 10.86 and 16.74 wt% in BP-AgNPs; part of the carbon comes from the conductive tape, and the remainder is consistent with the adsorbed layer identified by infrared spectroscopy above. Residual chlorine (0.91-1.02 wt%) and potassium (1.13-1.31 wt%) carried over from the extract. Quantitation by the ZAF standardless method is treated here as elemental confirmation rather than as an assay; the silver-equivalent content in Table 4 is the quantitative figure (Table 9, Fig. 2c-d).

Table 9. EDX elemental composition (ZAF standardless quantitative analysis)

Batch	Element	Mass (%)	Atom (%)
CO-AgNPs	C	12.41	36.17
	O	18.29	40.02
	Cl	1.02	1.01
	Ag	67.15	21.79
	K	1.13	1.01
BP-AgNPs	C	10.86	34.00
	O	16.74	39.29
	Cl	0.91	0.98

Batch	Element	Mass (%)	Atom (%)
	Ag	70.18	24.45
	K	1.31	1.28

Ag Lα signal at approximately 2.98 keV. Carbon arises partly from the conductive tape and partly from adsorbed phytochemicals; chlorine and potassium are extract carry-over.

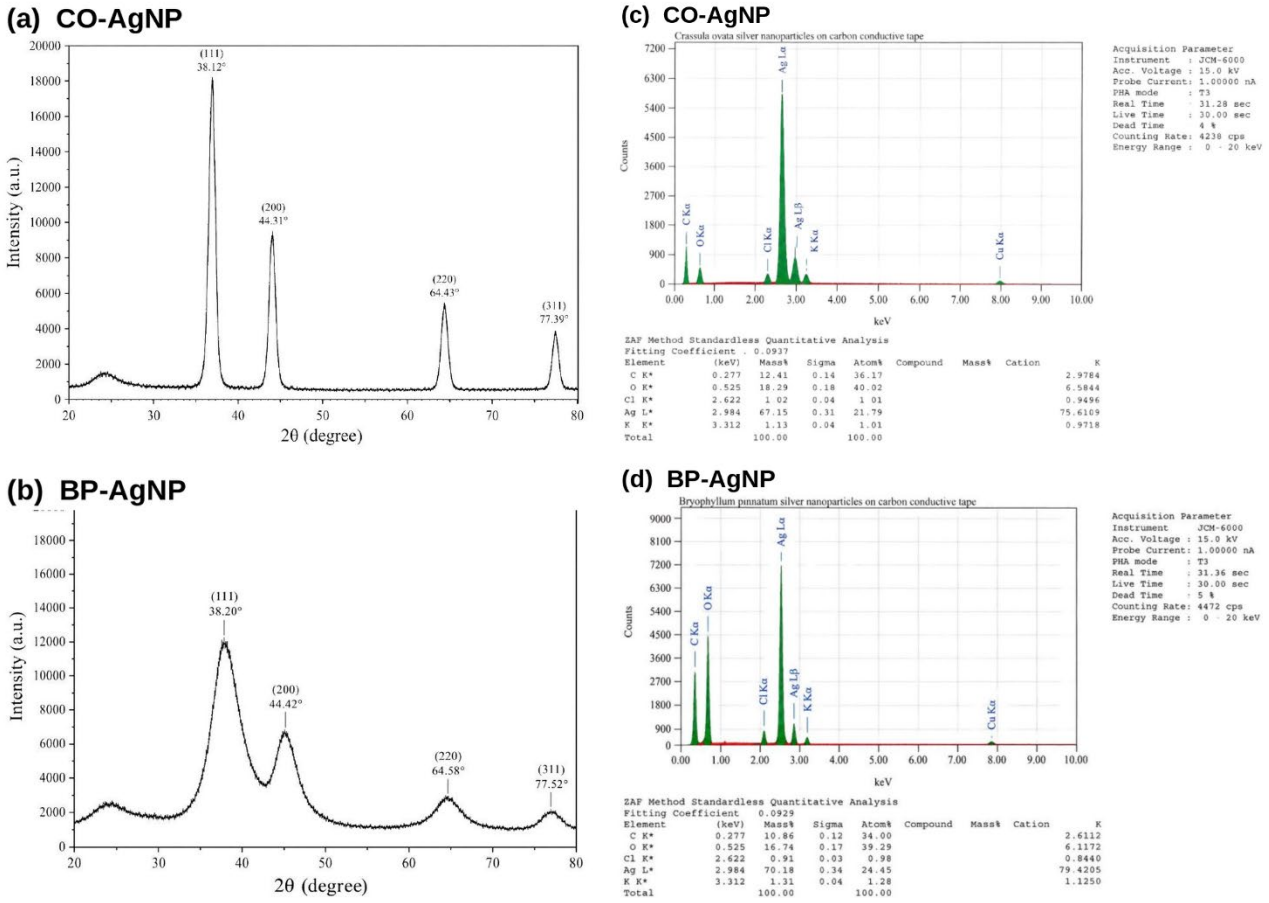

Figure 2. Crystalline phase and elemental composition. X-ray diffractograms over 2θ = 20-80° (Cu Kα, λ = 1.5406 Å) for (a) CO-AgNPs and (b) BP-AgNPs, with the (111), (200), (220) and (311) reflections of face-centred cubic silver indexed; panels are assigned from the 2θ values printed within each plot. Energy-dispersive X-ray spectra with ZAF standardless quantitation for (c) CO-AgNPs and (d) BP-AgNPs, acquired on carbon conductive tape at 15 kV, with the Ag Lα line near 2.98 keV dominant in both.

3.10 In vitro release

Both batches released silver-equivalent material steadily over 24 h with no burst phase. At 30 min, cumulative release was 8.53 ± 0.60% for CO-AgNPs and 9.87 ± 0.71% for BP-AgNPs; by 8 h the figures were 61.10 ± 2.07% and 66.93 ± 2.50%, and at 24 h 84.10 ± 2.55% and 88.60 ± 2.60%. Two-way ANOVA on the silver profiles gave $F(1,32) = 53.424$ for formulation and $F(7,32) = 1273.59$ for time, both $p < 0.0001$, with a non-significant interaction, $F(7,32) = 1.105$, $p = 0.3835$. Šídák-adjusted comparisons placed the difference between the two batches at 4, 6, 8 and 12 h, and the area under the curve from 0 to 24 h was 1503.70 ± 50.13 for CO-AgNPs against 1617.86 ± 55.15 for BP-AgNPs ($p = 0.0568$). The separation between the two profiles is therefore concentrated in the intermediate phase rather than in the endpoint (Table 10, Fig. 6a).

Table 10. Cumulative *in vitro* silver-equivalent release in phosphate-buffered saline pH 7.4 (mean ± SD, n = 3)

Time (h)	CO-AgNPs (%)	BP-AgNPs (%)	Difference (percentage points)
0.5	8.53 ± 0.60	9.87 ± 0.71	1.34
1	14.73 ± 1.06	17.17 ± 1.11	2.44
2	25.83 ± 1.39	28.70 ± 1.45	2.87
4	38.57 ± 1.65	43.23 ± 2.11	4.66
6	50.17 ± 1.80	55.77 ± 2.56	5.60
8	61.10 ± 2.07	66.93 ± 2.50	5.83
12	73.30 ± 2.35	78.63 ± 2.45	5.33
24	84.10 ± 2.55	88.60 ± 2.60	4.50

Two-way ANOVA: formulation $F(1,32) = 53.424$, $p < 0.0001$; time $F(7,32) = 1273.59$, $p < 0.0001$; formulation × time $F(7,32) = 1.105$, $p = 0.3835$. Šídák-adjusted comparisons were significant at 4, 6, 8 and 12 h. AUC0-24h 1503.70 ± 50.13 (CO-AgNPs) versus 1617.86 ± 55.15 (BP-AgNPs), $p = 0.0568$. The difference column is computed from the tabulated means.

3.11 DPPH radical scavenging

Converting either extract into its nanoparticle form roughly halved the IC50. CO-EXT scavenged with an IC50 of 106.13 µg/mL (95% CI 99.48-113.24) and BP-EXT with 79.56 µg/mL (76.11-83.16); the corresponding nanoparticles gave 57.46 µg/mL (54.29-60.81) and 46.14 µg/mL (44.01-48.36). MIX-AgNPs was the most active test material at 34.79 µg/mL (33.17-36.50). Ascorbic acid remained the strongest scavenger at 10.60 µg/mL. Hill slopes rose monotonically along the same series, from 1.101 for CO-EXT to 1.308 for MIX-AgNPs. Replicate-level R^2 for the five study treatments fell between 0.9796 and 0.9934. Two-way ANOVA returned $F(4,80) = 536.828$ for treatment, $F(7,80) = 3112.711$ for concentration and $F(28,80) = 19.880$ for the interaction, all $p < 0.0001$; the significant interaction means the spacing between treatments depends on dose, so the omnibus main effect is not used on its own to claim superiority at every concentration (Table 11, Fig. 6b).

Table 11. DPPH radical-scavenging concentration-response parameters

Treatment	IC50 (µg/mL)	95% CI	Hill slope	Replicate-level R^2	Fold change versus CO-EXT
CO-EXT	106.13	99.48-113.24	1.101	0.9796	1.00
BP-EXT	79.56	76.11-83.16	1.186	0.9907	1.33
CO-AgNPs	57.46	54.29-60.81	1.217	0.9884	1.85
BP-AgNPs	46.14	44.01-48.36	1.237	0.9926	2.30
MIX-AgNPs	34.79	33.17-36.50	1.308	0.9934	3.05
Ascorbic acid	10.60	10.22-10.99	1.351	0.9972	10.01

Ascorbic acid is an analytical reference control, not a test material. Fold change is computed from the tabulated IC50 values. Two-way ANOVA across the five study treatments: treatment $F(4,80) = 536.828$; concentration $F(7,80) = 3112.711$; interaction $F(28,80) = 19.880$; all $p < 0.0001$.

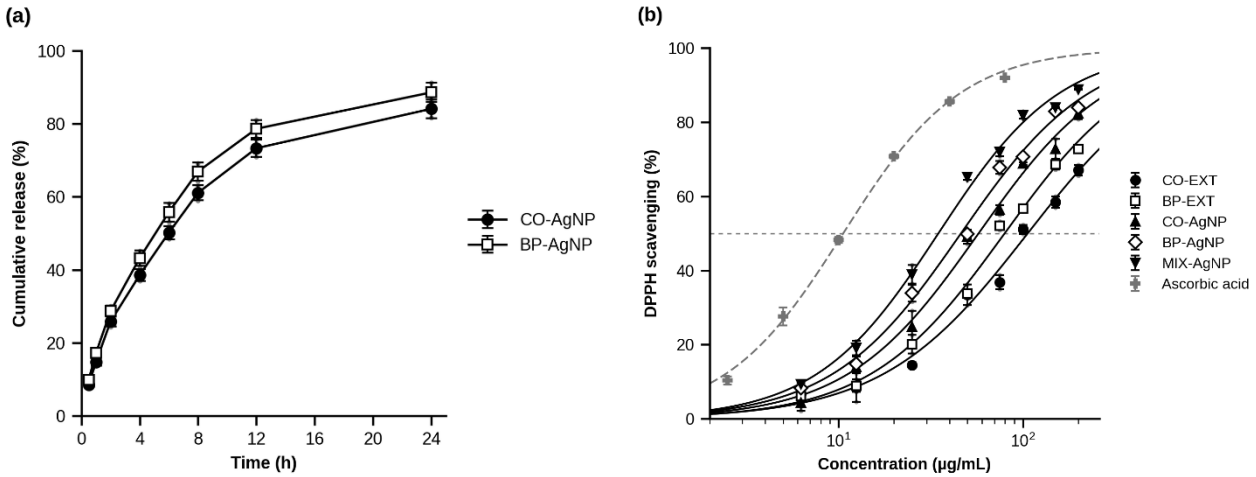

Figure 6. (a) Cumulative *in vitro* silver-equivalent release in phosphate-buffered saline pH 7.4 at 37 ± 0.5 °C; small grey points are individual replicates. (b) DPPH radical-scavenging concentration-response curves for the five study treatments with ascorbic acid as the analytical reference (grey, dashed); the horizontal dashed line marks 50% scavenging. Symbols are means with SD bars, n = 3, and curves are normalised variable-slope logistic fits to the replicate-level data.

3.12 Cytotoxicity

The same rank order held on all three cell lines. Against MCF-7, IC50 fell from 352.52 µg/mL (CO-EXT) and 230.28 µg/mL (BP-EXT) to 118.96 µg/mL (CO-AgNPs), 91.65 µg/mL (BP-AgNPs) and 65.68 µg/mL (MIX-AgNPs). HCT116 ran 445.58, 301.61, 147.46, 115.63 and 76.60 µg/mL across the same series, and A549 534.53, 349.21, 187.09, 138.31 and 89.00 µg/mL. Every value was bracketed inside the tested 6.25-800 µg/mL range, so none is an extrapolation. MCF-7 was the most responsive line and A549 the least, on every test material. Hill slopes were shallower for the extracts (0.857-0.910) than for the nanoparticle systems (0.992-1.312). Replicate-level R^2 ranged from 0.9640 to 0.9797 and reflects retained biological scatter. Two-way ANOVA was significant for treatment, concentration and their interaction on all three lines: MCF-7 $F(4,80) = 172.272$, $F(7,80) = 1154.585$ and $F(28,80) = 10.479$; HCT116 $F(4,80) = 184.407$, $F(7,80) = 1082.325$ and $F(28,80) = 11.471$; A549 $F(4,80) = 181.312$, $F(7,80) = 988.728$ and $F(28,80) = 10.307$, all $p < 0.0001$ (Table 12, Fig. 7).

Table 12. MTT cytotoxicity after 24 h exposure: IC50 values (µg/mL) with 95% confidence intervals and Hill slopes

Treatment	MCF-7	HCT116	A549
CO-EXT	352.52 (310.61-400.09); h = 0.872	445.58 (387.20-512.76); h = 0.872	534.53 (464.06-615.71); h = 0.910
BP-EXT	230.28 (205.25-258.36); h = 0.907	301.61 (265.63-342.47); h = 0.857	349.21 (308.45-395.36); h = 0.899
CO-AgNPs	118.96 (106.43-132.97); h = 1.098	147.46 (132.14-164.56); h = 1.020	187.09 (166.40-210.35); h = 0.992
BP-AgNPs	91.65 (82.04-102.38); h = 1.170	115.63 (102.48-130.46); h = 1.051	138.31 (123.67-154.70); h = 1.072
MIX-AgNPs	65.68 (58.87-73.28); h = 1.312	76.60 (68.53-85.62); h = 1.232	89.00 (79.29-99.90); h = 1.113

All IC50 values are bracketed within the tested 6.25-800 µg/mL range; none is extrapolated. Replicate-level R^2 ranged from 0.9640 to 0.9797. Two-way ANOVA was significant for treatment, concentration and their interaction on all three lines (all $p < 0.0001$).

Natural Resources for Human Health
eISSN: 2583-1194

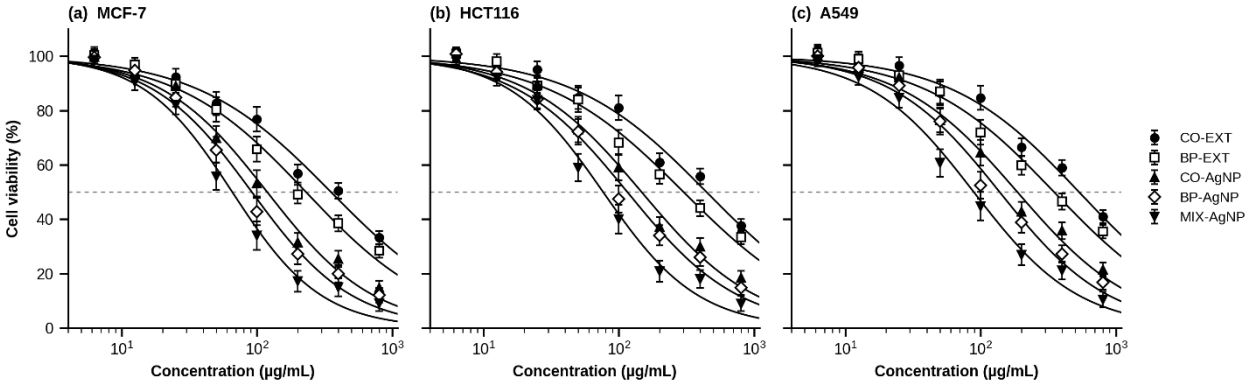

Figure 7. Cell viability after 24 h exposure: (a) MCF-7, (b) HCT116, (c) A549. Symbols are means with SD bars, n = 3; curves are normalised variable-slope logistic fits and the horizontal dashed line marks 50% viability. [FIGURE TO BE REPLACED ON RECEIPT OF THE SUPPLIED MTT IMAGE SET.]

3.13 Macrophage viability and cytokine suppression

The viability plate was run first, because cytokine loss from a dying macrophage is not an anti-inflammatory effect. Across the 3.125-50 µg/mL range every treatment held mean viability at or above 80%. The lowest value was MIX-AgNPs at 50 µg/mL, 80.80 ± 4.08%, which sits immediately above the prespecified threshold and is flagged accordingly; BP-AgNPs at the same concentration gave 81.90 ± 2.82% and CO-AgNPs 84.10 ± 3.42%. Lipopolysaccharide alone left viability at 95.40 ± 1.91% and dexamethasone at 97.20 ± 1.75% (Table 14, Fig. 8).

Table 13. RAW 264.7 macrophage viability under the anti-inflammatory treatment conditions (mean ± SD, n = 3)

Treatment	3.125 µg/mL	6.25 µg/mL	12.5 µg/mL	25 µg/mL	50 µg/mL
CO-EXT	101.20 ± 2.12	99.10 ± 2.67	97.30 ± 2.51	94.00 ± 2.78	89.80 ± 2.78
BP-EXT	100.40 ± 2.61	98.20 ± 3.20	95.60 ± 3.26	91.80 ± 3.05	87.40 ± 2.88
CO-AgNPs	99.60 ± 3.22	96.80 ± 4.16	93.40 ± 3.76	88.90 ± 3.52	84.10 ± 3.42
BP-AgNPs	99.00 ± 4.85	95.80 ± 3.93	91.60 ± 3.53	86.70 ± 3.74	81.90 ± 2.82
MIX-AgNPs	98.50 ± 4.93	94.90 ± 4.73	90.50 ± 4.69	85.20 ± 3.13	80.80 ± 4.08

Values are percentage viability against the unstimulated control. Lipopolysaccharide alone gave 95.40 ± 1.91% and dexamethasone 1 µM gave 97.20 ± 1.75%. The prespecified interpretability threshold was 80%; MIX-AgNP at 50 µg/mL sits immediately above it and is flagged as borderline.

Lipopolysaccharide raised TNF-α from 36.45 ± 3.36 pg/mL in unstimulated cells to 751.94 ± 31.40 pg/mL, and IL-6 from 25.75 ± 3.25 to 901.90 ± 55.33 pg/mL; dexamethasone brought them down to 198.12 ± 12.82 and 234.34 ± 16.95 pg/mL. At 50 µg/mL, TNF-α inhibition was 37.36 ± 3.10% for CO-EXT, 47.33 ± 3.32% for BP-EXT, 60.74 ± 3.62% for CO-AgNPs, 68.79 ± 3.27% for BP-AgNPs and 75.07 ± 2.06% for MIX-AgNPs. IL-6 inhibition at the same concentration ran 39.10 ± 3.75%, 49.31 ± 3.05%, 62.10 ± 3.29%, 68.64 ± 2.23% and 75.05 ± 2.33%. Apparent 50% inhibitory concentrations followed the same order, but the two extracts extrapolate beyond the highest tested concentration on both analytes and are labelled as such rather than treated as measured potencies (Table 12, Fig. 8).

Natural Resources for Human Health
eISSN: 2583-1194

Table 14. Cytokine inhibition in lipopolysaccharide-stimulated RAW 264.7 macrophages

Treatment	TNF-α inhibition at 50 µg/mL (%)	TNF-α apparent IC50 (µg/mL)	IL-6 inhibition at 50 µg/mL (%)	IL-6 apparent IC50 (µg/mL)
CO-EXT	37.36 ± 3.10	77.68 (extrapolated)	39.10 ± 3.75	81.14 (extrapolated)
BP-EXT	47.33 ± 3.32	54.07 (extrapolated)	49.31 ± 3.05	50.47 (extrapolated)
CO-AgNPs	60.74 ± 3.62	32.58 (28.28-36.87)	62.10 ± 3.29	31.32 (26.63-36.00)
BP-AgNPs	68.79 ± 3.27	23.12 (20.17-26.06)	68.64 ± 2.23	22.35 (19.73-24.97)
MIX-AgNPs	75.07 ± 2.06	17.81 (15.64-19.98)	75.05 ± 2.33	16.33 (14.45-18.21)

Apparent IC50 values above the highest tested concentration of 50 µg/mL are extrapolated estimates and are not treated as experimentally bracketed potencies. Reference values: lipopolysaccharide alone raised TNF-α to 751.94 ± 31.40 pg/mL and IL-6 to 901.90 ± 55.33 pg/mL; dexamethasone 1 µM gave 198.12 ± 12.82 and 234.34 ± 16.95 pg/mL.

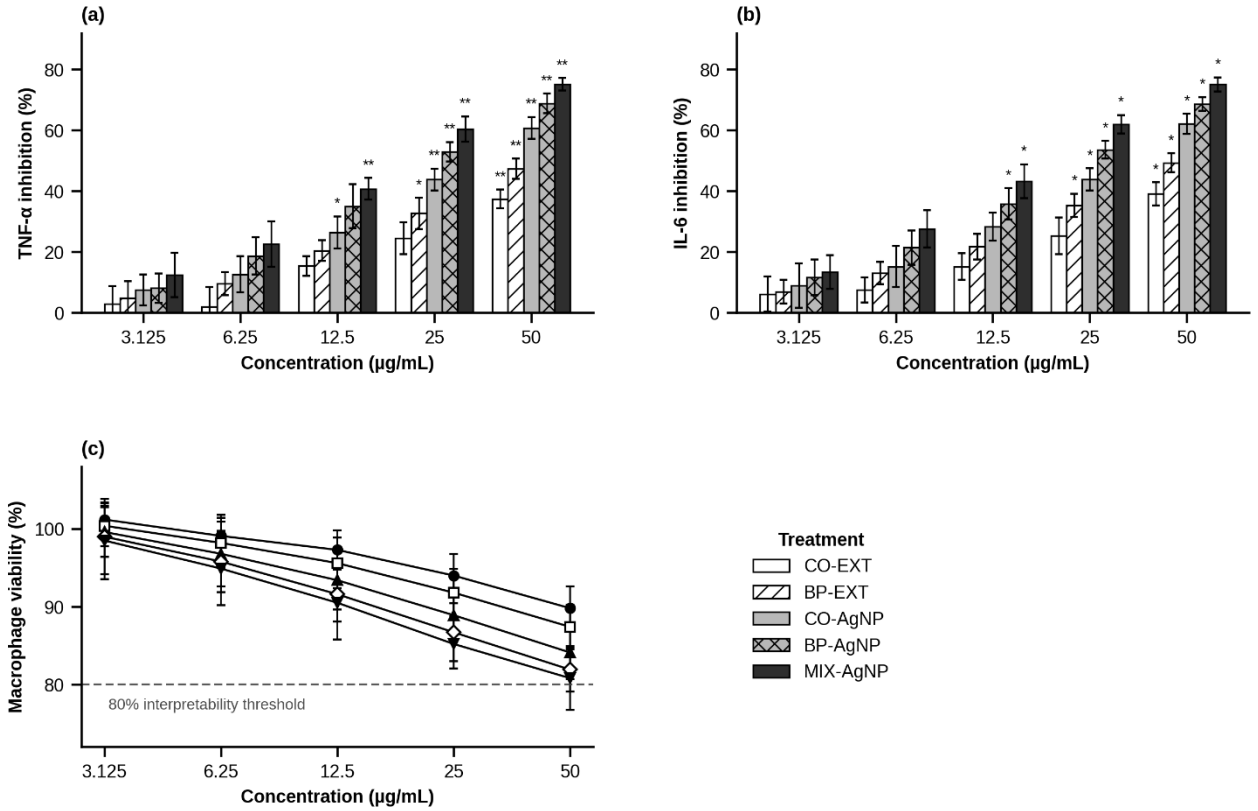

Figure 8. Anti-inflammatory evaluation in lipopolysaccharide-stimulated RAW 264.7 macrophages: (a) TNF-α inhibition, (b) IL-6 inhibition, (c) parallel macrophage viability with the 80% interpretability threshold marked. Bars and symbols are means with SD bars, n = 3. Significance codes above bars are Holm-adjusted Welch comparisons against the LPS control (* $p < 0.05$, ** $p < 0.01$).

Two-way ANOVA gave $F(4,50) = 65.822$ for treatment, $F(4,50) = 269.431$ for concentration and $F(16,50) = 3.090$ for the interaction on TNF-α ($p < 0.0001$, $p < 0.0001$ and $p = 0.0012$), and $F(4,50) = 69.604$, $F(4,50) = 272.071$ and $F(16,50) = 3.399$ on IL-6 ($p < 0.0001$, $p < 0.0001$ and $p = 0.0005$). Against the LPS control after Holm adjustment, the nanoparticle systems separated from control at lower concentrations than the extracts: MIX-AgNPs from 12.5 µg/mL on both analytes, CO-AgNPs

from 12.5 µg/mL on TNF-α and 25 µg/mL on IL-6, BP-AgNPs from 25 and 12.5 µg/mL, while CO-EXT reached significance only at 50 µg/mL. Direct comparison of MIX-AgNPs against the individual nanoparticle systems at matched concentrations produced one adjusted p value below 0.05 out of ten tests, MIX against CO-AgNPs for IL-6 at 25 µg/mL ($p = 0.0297$); MIX was not significantly different from BP-AgNPs at any matched concentration on either analyte.

3.14 Cross-assay summary

Six independent readouts, one order. The potency sequence MIX-AgNPs > BP-AgNPs > CO-AgNPs > BP-EXT > CO-EXT held for radical scavenging, for cytotoxicity on each of MCF-7, HCT116 and A549, and for suppression of both TNF-α and IL-6 (Table 15). The ratio between the weakest and strongest test material was 3.05-fold for DPPH, 5.37-fold for MCF-7, 5.82-fold for HCT116, 6.01-fold for A549, 4.36-fold for TNF-α and 4.97-fold for IL-6.

Table 15. Cross-assay IC50 summary (µg/mL); lower values indicate greater activity

Assay	CO-EXT	BP-EXT	CO-AgNPs	BP-AgNPs	MIX-AgNPs	Weakest / strongest
DPPH	106.13	79.56	57.46	46.14	34.79	3.05
MTT, MCF-7	352.52	230.28	118.96	91.65	65.68	5.37
MTT, HCT116	445.58	301.61	147.46	115.63	76.60	5.82
MTT, A549	534.53	349.21	187.09	138.31	89.00	6.01
TNF-α inhibition	77.68	54.07	32.58	23.12	17.81	4.36
IL-6 inhibition	81.14	50.47	31.32	22.35	16.33	4.97

Cytokine values are apparent inhibitory concentrations; the two extract values on each analyte are extrapolated above the 50 µg/mL ELISA range. The final column is computed from the tabulated values.

4. DISCUSSION

The two extracts produced measurably different particles from an identical reaction. The 4.4 nm red shift in plasmon position for BP-AgNPs, together with its wider band, points to a broader distribution of particle sizes and shapes rather than to larger particles, since plasmon position and width in colloidal silver depend jointly on size, geometry and the dielectric environment set by the capping layer (Huang & Xu, 2010; Bhardwaj et al., 2018). Both peak positions fall in the same window reported for silver nanoparticles reduced by fungal, actinomycete and plant biomass under comparable conditions (Faisal et al., 2020; Eid et al., 2020; Kamradgi et al., 2022; Constantin et al., 2023). Light scattering supports that reading: BP-AgNPs was the smaller of the two by hydrodynamic diameter and the narrower by polydispersity index, so the extra band width is more plausibly a shape and capping effect than a size effect.

Zeta potential ran in the same direction. BP-AgNPs carried −32.57 ± 0.80 mV against −28.37 ± 0.75 mV for CO-AgNPs, and the difference is consistent with the two phytochemical profiles. *B. pinnatum* leaf is dominated by polar quercetin- and kaempferol-type glycosides carrying multiple sugar units, with bufadienolides alongside them (Fürer et al., 2013; Oufir et al., 2015), and a denser layer of ionisable phenolic and carboxylate groups on the particle surface would give both a more negative surface charge and tighter growth control. The higher 70% ethanol extractive value for *B. pinnatum* recorded in this study is consistent with the larger soluble polar pool. Surface charge is not a cosmetic parameter here, since it governs colloidal stability and, once the particles reach a protein-containing medium, the composition of the adsorbed corona and hence cellular uptake (Bhattacharjee, 2016; Arezki et al., 2022).

Crystallite size from the Debye-Scherrer relation was smaller than the hydrodynamic diameter for both batches, 29.75 nm against 83.83 nm for CO-AgNPs and 23.87 nm against 75.57 nm for BP-AgNPs. The two numbers are not interchangeable. Diffraction reports the size of a coherently diffracting domain, while dynamic light scattering reports the diameter of the particle plus its capping shell and hydration layer as it diffuses. A polycrystalline particle with an adsorbed organic coat will always read larger by scattering, and the gap is wider for CO-AgNPs, which also had the higher polydispersity index. The unindexed broad

background between 20° and 35° in both diffractograms, stronger in BP-AgNPs, is the same organic material seen from a different instrument.

Elemental analysis puts a number on that coat. Silver accounted for 67.15 and 70.18 wt%, with carbon and oxygen making up most of the remainder. Some of that carbon is the conductive tape, but the oxygen fraction of 16.74-18.29 wt% cannot be explained that way and is consistent with the oxygenated phytochemicals that donated electrons during reduction and stayed adsorbed afterwards, the mechanism described across the plant-mediated synthesis literature (Sharma et al., 2009; Patil & Kim, 2017; Huq et al., 2022; Thomas et al., 2024). Residual chlorine and potassium at roughly 1 wt% each are carry-over from the extract, which is expected given the mineral load of crassulacean acid metabolism leaf tissue.

The release experiment needs to be read for what it is. It measures silver-equivalent material crossing a 12-14 kDa membrane and quantified by plasmon absorbance, which is a surrogate for the mobile fraction and not a speciation measurement. Both batches released steadily to 84-89% over 24 h with no burst, and the profiles separated at 4-12 h before converging by 24 h, which is why the formulation effect was significant while the interaction term was not. The mechanistic importance of the mobile fraction is well established: oxidative dissolution of metallic silver to Ag^+ is a cooperative process requiring dissolved oxygen and protons, and its rate depends on pH, temperature and the presence of organic ligands (Liu & Hurt, 2010). Toxicity of silver nanoparticles in several model systems correlates with dissolved silver rather than with particle size alone, though dissolution at the cell interface, and inside the cell after uptake, can contribute more than the concentration measured in the bulk medium (McQuillan et al., 2012; Yang et al., 2012; Zhang & Wang, 2023). The present data cannot separate those routes, since dissolved Ag^+ was not measured by an element-specific method.

On the biological side, the most useful feature of the dataset is that one rank order survived six readouts that have no shared assay chemistry: a colorimetric radical reaction, three tetrazolium reduction assays on different cell lines, and two sandwich immunoassays. That consistency is difficult to attribute to interference in any single platform, particularly since material-matched blanks were subtracted at every concentration in both the DPPH and the MTT arms, which is the control that particle-interference studies specifically call for (Holder et al., 2012; Tournebize et al., 2013).

Radical-scavenging potency improved by 1.85-fold for *C. ovata* and 1.72-fold for *B. pinnatum* on conversion to the nanoparticle form. Two contributions are plausible and the present data do not separate them: polyphenols retained on the particle surface remain redox-active, and the metallic surface itself can participate in electron transfer with the DPPH radical. Both parent extracts were active in the range expected for flavonol-glycoside-rich material, and both fall in the tens of micrograms per millilitre band that crude polar plant extracts typically occupy when DPPH and tetrazolium endpoints are run side by side (Ahmad et al., 2005). The higher activity of BP-EXT over CO-EXT matches the structure-activity pattern for flavonoids, where the B-ring catechol arrangement of quercetin-type compounds confers stronger scavenging than kaempferol-type substitution (Silva et al., 2002; Torres Castañeda et al., 2016; Gulcin, 2020). Ascorbic acid stayed 3.3-fold more potent than the best nanoparticle system, which is the correct place for a small-molecule reference control in this assay.

Cytotoxicity values sit within the band reported for plant-mediated silver nanoparticles, though comparison across studies is loose because exposure time, seeding density and dose spacing vary. Published IC50 figures for biogenic silver nanoparticles against MCF-7 and A549 span roughly one to two orders of magnitude depending on the source plant and the assay (Sankar et al., 2013; Elangovan et al., 2015; Castro-Aceituno et al., 2016; Bethu et al., 2018; Devanesan et al., 2021; Mani et al., 2021; Dağlıoğlu et al., 2023). The line ranking observed here, with MCF-7 most responsive and A549 least, is a common but not universal pattern. Mechanistic work on biogenic silver nanoparticles converges on reactive oxygen species generation, mitochondrial membrane depolarisation and caspase activation, with downstream shifts in Bax/Bcl-2 balance and p53 (Buttacavoli et al., 2018; Cameron et al., 2018; De Matteis et al., 2018; Hamida et al., 2020; Raja et al., 2020; Mohamed et al., 2022; Nguyen et al., 2022; Ren et al., 2022; Vahabirad et al., 2024). None of those endpoints was measured here, so the present study establishes a potency ranking and not a mechanism. It is also worth noting that ethanolic *K. pinnata* leaf extract has been reported to act on cancer cells through ROS-induced apoptosis with selectivity against a normal colon line (Faundes-Gandolfo et al., 2024), which makes the parent extract a reasonable starting point but does not transfer to the nanoparticle form without direct evidence.

Cytokine suppression is the arm where the viability control does the most work. Both nanoparticle systems and the mixture reduced TNF-α and IL-6 in a concentration-dependent way while macrophage viability stayed at or above 80%, so the effect is

not simply fewer live cells producing less cytokine. Silver nanoparticles have been shown to lower TNF-α and IL-6 output from stimulated or infected macrophages in several independent systems, including polyvinylpyrrolidone-stabilised particles, dendrimer-encapsulated particles, surface-functionalised particles and particle-coated sutures (Yilma et al., 2013; Liu et al., 2014; Liu et al., 2017; Kumawat et al., 2022). The lipopolysaccharide challenge used here signals through TLR4 and NF-ϰB, and plant flavonoids can act at that pathway in the same cell model (Fu et al., 2021), which offers a route by which surface-retained flavonoids and the metallic surface could contribute jointly. That remains an inference: NF-ϰB translocation, iNOS and COX-2 expression and nitric oxide output were not measured.

On the combination arm the conclusion is deliberately narrow. MIX-AgNPs gave the lowest fitted IC50 on all six readouts and the largest numerical cytokine reduction, but after correction for multiple comparisons it separated from CO-AgNPs at one concentration on one analyte and never separated from BP-AgNPs. A lower mean or a lower fitted IC50 at a single fixed ratio is not evidence of interaction; establishing synergy requires a ratio-design experiment and a formal interaction model such as the median-effect combination index (Chou, 2010), which has been applied to silver nanoparticle combinations elsewhere (Rivera et al., 2024). The result is therefore reported as enhanced activity of the 1:1 physical mixture, and the design that would settle the question is set out below.

Several limitations bear on interpretation. Dissolved silver was not quantified by an element-specific method, so the relative contribution of particulate and ionic silver to the biological effects cannot be apportioned. No free silver nitrate arm was carried through the biological panel, which would be the direct control for that question. The physical mixture was characterised only by the properties of its two components and not as a mixed dispersion, so hetero-aggregation on mixing cannot be excluded. Cytotoxicity was assessed against three cancer lines without a matched non-tumour line, so no selectivity index is available, and no reference cytotoxic drug was run alongside. Colloidal stability was measured at a single time point rather than over storage or in serum-containing medium. Mechanistic endpoints for both the cytotoxic and the anti-inflammatory effect were outside the present scope. Finally, MIX-AgNPs at 50 µg/mL sat immediately above the 80% viability threshold in the macrophage arm, so the 25 µg/mL level gives the cleaner high-dose anti-inflammatory comparison.

Two further points are worth recording for anyone extending this work. *B. pinnatum* contains bufadienolides, and genotoxicity signals have been reported for ethanolic leaf extract in the mouse lymphoma and *in vivo* micronucleus assays, with weaker signals from fresh leaf juice in human lymphocytes (Saravanan et al., 2020; Bhavsar & Chandel, 2022; Sharma et al., 2024). Any translational development of BP-AgNPs should therefore carry a genotoxicity package rather than rely on the cytotoxicity data alone. Separately, the raw-material constants reported in Table 1 should be treated as batch-specific: metabolite content in *Crassulaceae* leaf varies with harvest date, leaf age and growing location by factors of three or more for bufadienolides (Oufir et al., 2015), which is the standard argument for fingerprint-based release testing of plant starting material (Tetali et al., 2021).

4. CONCLUSION

Ethanolic leaf extracts of *C. ovata* and *B. pinnatum* both reduced silver nitrate to face-centred cubic silver nanoparticles under one fixed protocol, and the two products differed in ways that track the chemistry of the source plant: BP-AgNPs was smaller (75.57 ± 1.25 nm against 83.83 ± 1.25 nm), more narrowly distributed (polydispersity index 0.252 against 0.294), more negatively charged (−32.57 mV against −28.37 mV), of smaller crystallite size (23.87 nm against 29.75 nm) and higher in silver content by both EDX and UV quantitation. Across radical scavenging, cytotoxicity on MCF-7, HCT116 and A549, and TNF-α and IL-6 suppression in stimulated RAW 264.7 macrophages, the potency order was identical on every readout: MIX-AgNPs > BP-AgNPs > CO-AgNPs > BP-EXT > CO-EXT. Conversion of either extract into its nanoparticle form improved potency by 1.7- to 3.0-fold depending on the endpoint. The 1:1 physical mixture was the most active material tested but was not statistically superior to BP-AgNPs at matched concentrations after multiplicity adjustment, and is reported as showing enhanced activity rather than synergy. A ratio-design combination study with a formal interaction model, an ionic silver control arm, a non-tumour reference line and element-specific measurement of dissolved silver are the next steps indicated by these results.

5.ACKNOWLEDGEMENT

The authors sincerely acknowledge the department of pharmaceutical sciences, school of pharmacy, itm university, gwalior, madhya pradesh, india, for providing the necessary facilities and support to carry out this research work. The authors also express their sincere gratitude to dr. Tirthankar choudhury, research supervisor, for his valuable guidance, encouragement, and

support throughout the study. The authors are also thankful to the central national herbarium, botanical survey of india (bsi), shibpur, howrah, for authentication of the plant materials used in this study.acknowledgement

Author contributions

Somendra kumar: conceptualization, methodology, investigation, experimentation, data collection, data analysis, and writing—original draft.

Dr. Tirthankar choudhury: supervision, conceptual guidance, validation, critical review, and editing of the manuscript.

All authors have read and approved the final version of the manuscript.author contributions

Conflict of interest

The authors declare that they have no conflicts of interest related to the publication of this manuscript.

Ethics statement

This study involved only in-vitro experiments and did not involve human participants or animals. Therefore, ethical approval was not required for this study.

Data availability statement

The data generated and analyzed during the current study are available from the corresponding author upon reasonable request.

REFERENCES

[1] Ahmad, R., Ali, A. M., Israf, D. A., Ismail, N. H., Shaari, K., & Lajis, N. H. (2005). Antioxidant, radical-scavenging, anti-inflammatory, cytotoxic and antibacterial activities of methanolic extracts of some Hedyotis species. Life Sciences, 76(17), 1953-1964. https://doi.org/10.1016/j.lfs.2004.08.039

[2] Arezki, Y., Delalande, F., Schaeffer-Reiss, C., Cianférani, S., Rapp, M., Lebeau, L., Pons, F., & Ronzani, C. (2022). Surface charge influences protein corona, cell uptake and biological effects of carbon dots. Nanoscale, 14(39), 14695-14710. https://doi.org/10.1039/d2nr03611h

[3] Bachmann, S., Betschart, C., Gerber, J., Fürer, K., Mennet, M., Hamburger, M., Potterat, O., von Mandach, U., & Simões-Wüst, A. P. (2017). Potential of *Bryophyllum pinnatum* as a detrusor relaxant: An *in vitro* exploratory study. Planta Medica, 83(16), 1274-1280. https://doi.org/10.1055/s-0043-109097

[4] Bethu, M. S., Netala, V. R., Domdi, L., Tartte, V., & Janapala, V. R. (2018). Potential anticancer activity of biogenic silver nanoparticles using leaf extract of Rhynchosia suaveolens: An insight into the mechanism. Artificial Cells, Nanomedicine, and Biotechnology, 46(sup1), 104-114. https://doi.org/10.1080/21691401.2017.1414824

[5] Bhardwaj, A. K., Shukla, A., Maurya, S., Singh, S. C., Uttam, K. N., Sundaram, S., Singh, M. P., & Gopal, R. (2018). Direct sunlight enabled photo-biochemical synthesis of silver nanoparticles and their bactericidal efficacy: Photon energy as key for size and distribution control. Journal of Photochemistry and Photobiology B: Biology, 188, 42-49. https://doi.org/10.1016/j.jphotobiol.2018.08.019

[6] Bhattacharjee, S. (2016). DLS and zeta potential - What they are and what they are not? Journal of Controlled Release, 235, 337-351. https://doi.org/10.1016/j.jconrel.2016.06.017

[7] Bhavsar, S., & Chandel, D. (2022). Cytotoxic and genotoxic effects of *Kalanchoe pinnata* (Lam.) Pers. fresh leaf juice in the cultured human blood lymphocytes. Drug and Chemical Toxicology, 45(1), 360-366. https://doi.org/10.1080/01480545.2019.1696814

[8] Buttacavoli, M., Albanese, N. N., Di Cara, G., Alduina, R., Faleri, C., Gallo, M., Pizzolanti, G., Gallo, G., Feo, S., Baldi, F., & Cancemi, P. (2018). Anticancer activity of biogenerated silver nanoparticles: An integrated proteomic investigation. Oncotarget, 9(11), 9685-9705. https://doi.org/10.18632/oncotarget.23859

[9] Cameron, S. J., Hosseinian, F., & Willmore, W. G. (2018). A current overview of the biological and cellular effects of nanosilver. International Journal of Molecular Sciences, 19(7), 2030. https://doi.org/10.3390/ijms19072030

[10] Castro-Aceituno, V., Ahn, S., Simu, S. Y., Singh, P., Mathiyalagan, R., Lee, H. A., & Yang, D. C. (2016). Anticancer activity of silver nanoparticles from Panax ginseng fresh leaves in human cancer cells. Biomedicine & Pharmacotherapy, 84, 158-165. https://doi.org/10.1016/j.biopha.2016.09.016

[11] Chou, T.-C. (2010). Drug combination studies and their synergy quantification using the Chou-Talalay method. Cancer Research, 70(2), 440-446. https://doi.org/10.1158/0008-5472.CAN-09-1947

[12] Constantin, M., Răut, I., Suica-Bunghez, R., Firincă, C., Radu, N., Gurban, A.-M., Preda, S., Alexandrescu, E., Doni, M., & Jecu, L. (2023). Ganoderma lucidum-mediated green synthesis of silver nanoparticles with antimicrobial activity. Materials, 16(12), 4261. https://doi.org/10.3390/ma16124261

[13] Coutinho, M. A. S., Casanova, L. M., Nascimento, L. B. S., Leal, D., Palmero, C., Toma, H. K., dos Santos, E. P., Nasciutti, L. E., & Costa, S. S. (2021). Wound healing cream formulated with *Kalanchoe pinnata* major flavonoid is as effective as the aqueous leaf extract cream in a rat model of excisional wound. Natural Product Research, 35(24), 6034-6039. https://doi.org/10.1080/14786419.2020.1817012

[14] Dağlıoğlu, Y., Öztürk, B. Y., & Khatami, M. (2023). Apoptotic, cytotoxic, antioxidant, and antibacterial activities of biosynthesized silver nanoparticles from nettle leaf. Microscopy Research and Technique, 86(6), 669-685. https://doi.org/10.1002/jemt.24306

[15] De Matteis, V., Cascione, M., Toma, C. C., & Leporatti, S. (2018). Silver nanoparticles: Synthetic routes, *in vitro* toxicity and theranostic applications for cancer disease. Nanomaterials, 8(5), 319. https://doi.org/10.3390/nano8050319

[16] Devanesan, S., Jayamala, M., AlSalhi, M. S., Umamaheshwari, S., & Ranjitsingh, A. J. A. (2021). Antimicrobial and anticancer properties of Carica papaya leaves derived di-methyl flubendazole mediated silver nanoparticles. Journal of Infection and Public Health, 14(5), 577-587. https://doi.org/10.1016/j.jiph.2021.02.004

[17] Eid, A. M., Fouda, A., Niedbała, G., Hassan, S. E.-D., Salem, S. S., Abdo, A. M., Hetta, H. F., & Shaheen, T. I. (2020). Endophytic Streptomyces laurentii mediated green synthesis of Ag-NPs with antibacterial and anticancer properties for developing functional textile fabric properties. Antibiotics, 9(10), 641. https://doi.org/10.3390/antibiotics9100641

[18] Elangovan, K., Elumalai, D., Anupriya, S., Shenbhagaraman, R., Kaleena, P. K., & Murugesan, K. (2015). Phyto mediated biogenic synthesis of silver nanoparticles using leaf extract of Andrographis echioides and its bio-efficacy on anticancer and antibacterial activities. Journal of Photochemistry and Photobiology B: Biology, 151, 118-124. https://doi.org/10.1016/j.jphotobiol.2015.05.015

[19] Faisal, S., Shah, S. A., Shah, S., Akbar, M. T., Jan, F., Haq, I., Baber, M. E., Aman, K., Zahir, F., Bibi, F., Syed, F., Iqbal, M., Jawad, S. M., & Salman, S. (2020). Biomedical and photo-catalytic application of bio-inspired Zingiber officinale mediated silver nanoparticles. Journal of Biomedical Nanotechnology, 16(4), 492-504. https://doi.org/10.1166/jbn.2020.2918

[20] Faundes-Gandolfo, N., Jara-Gutiérrez, C., Párraga, M., Montenegro, I., Vera, W., Escobar, M., Madrid, A., Valenzuela-Valderrama, M., & Villena, J. (2024). *Kalanchoe pinnata* (Lam.) Pers. leaf ethanolic extract exerts selective anticancer activity through ROS-induced apoptotic cell death in human cancer cell lines. BMC Complementary Medicine and Therapies, 24(1), 269. https://doi.org/10.1186/s12906-024-04570-7

[21] Fu, Y.-J., Xu, B., Huang, S.-W., Luo, X., Deng, X.-L., Luo, S., Liu, C., Wang, Q., Chen, J.-Y., & Zhou, L. (2021). Baicalin prevents LPS-induced activation of TLR4/NF-kappaB p65 pathway and inflammation in mice via inhibiting the expression of CD14. Acta Pharmacologica Sinica, 42(1), 88-96. https://doi.org/10.1038/s41401-020-0411-9

[22] Fürer, K., Eberli, D., Betschart, C., Brenneisen, R., De Mieri, M., Hamburger, M., Mennet-von Eiff, M., Potterat, O., Schnelle, M., Simões-Wüst, A. P., & von Mandach, U. (2015). Inhibition of porcine detrusor contractility by the flavonoid fraction of *Bryophyllum pinnatum* - A potential phytotherapeutic drug for the treatment of the overactive bladder syndrome. Phytomedicine, 22(1), 158-164. https://doi.org/10.1016/j.phymed.2014.11.009

[23] Fürer, K., Raith, M., Brenneisen, R., Mennet, M., Simões-Wüst, A. P., von Mandach, U., Hamburger, M., & Potterat, O. (2013). Two new flavonol glycosides and a metabolite profile of *Bryophyllum pinnatum*, a phytotherapeutic used in obstetrics and gynaecology. Planta Medica, 79(16), 1565-1571. https://doi.org/10.1055/s-0033-1350808

[24] Fürer, K., Simões-Wüst, A. P., von Mandach, U., Hamburger, M., & Potterat, O. (2016). *Bryophyllum pinnatum* and related species used in anthroposophic medicine: Constituents, pharmacological activities, and clinical efficacy. Planta Medica, 82(11-12), 930-941. https://doi.org/10.1055/s-0042-106727

[25] Gilman, I. S., & Edwards, E. J. (2020). Crassulacean acid metabolism. Current Biology, 30(2), R57-R62. https://doi.org/10.1016/j.cub.2019.11.073

[26] Gulcin, İ. (2020). Antioxidants and antioxidant methods: An updated overview. Archives of Toxicology, 94(3), 651-715. https://doi.org/10.1007/s00204-020-02689-3

[27] Hamida, R. S., Albasher, G., & Bin-Meferij, M. M. (2020). Oxidative stress and apoptotic responses elicited by Nostoc-synthesized silver nanoparticles against different cancer cell lines. Cancers, 12(8), 2099. https://doi.org/10.3390/cancers12082099

[28] Hernández-Caballero, M. E., Sierra-Ramírez, J. A., Villalobos-Valencia, R., & Seseña-Méndez, E. (2022). Potential of *Kalanchoe pinnata* as a cancer treatment adjuvant and an epigenetic regulator. Molecules, 27(19), 6425. https://doi.org/10.3390/molecules27196425

[29] Holder, A. L., Goth-Goldstein, R., Lucas, D., & Koshland, C. P. (2012). Particle-induced artifacts in the MTT and LDH viability assays. Chemical Research in Toxicology, 25(9), 1885-1892. https://doi.org/10.1021/tx3001708

[30] Huang, T., & Xu, X.-H. N. (2010). Synthesis and characterization of tunable rainbow coloured colloidal silver nanoparticles using single-nanoparticle plasmonic microscopy and spectroscopy. Journal of Materials Chemistry, 20(44), 9867-9876. https://doi.org/10.1039/C0JM01990A

[31] Huq, M. A., Ashrafudoulla, M., Rahman, M. M., Balusamy, S. R., & Akter, S. (2022). Green synthesis and potential antibacterial applications of bioactive silver nanoparticles: A review. Polymers, 14(4), 742. https://doi.org/10.3390/polym14040742

[32] Indian Pharmacopoeia Commission. (2022). Indian Pharmacopoeia 2022 (Appendices 2.2.32, 2.3.19 and 2.4.16). Government of India, Ministry of Health and Family Welfare.

[33] International Organization for Standardization. (2009). ISO 10993-5:2009. Biological evaluation of medical devices - Part 5: Tests for *in vitro* cytotoxicity. ISO.

[34] Kamradgi, S., Babanagare, S., & Gunagambhire, V. (2022). Characterization of Talaromyces islandicus-mediated silver nanoparticles and evaluation of their antibacterial and anticancer potential. Microscopy Research and Technique, 85(5), 1825-1836. https://doi.org/10.1002/jemt.24044

[35] Kumawat, M., Madhyastha, H., Singh, M., Revaprasadu, N., Srinivas, S. P., & Daima, H. K. (2022). Double functionalized haemocompatible silver nanoparticles control cell inflammatory homeostasis. PLoS ONE, 17(10), e0276296. https://doi.org/10.1371/journal.pone.0276296

[36] Liu, J., & Hurt, R. H. (2010). Ion release kinetics and particle persistence in aqueous nano-silver colloids. Environmental Science & Technology, 44(6), 2169-2175. https://doi.org/10.1021/es9035557

[37] Liu, X., Gao, P., Du, J., Zhao, X., & Wong, K. K. Y. (2017). Long-term anti-inflammatory efficacy in intestinal anastomosis in mice using silver nanoparticle-coated suture. Journal of Pediatric Surgery, 52(12), 2083-2087. https://doi.org/10.1016/j.jpedsurg.2017.08.026

[38] Liu, X., Hao, W., Lok, C.-N., Wang, Y. C., Zhang, R., & Wong, K. K. Y. (2014). Dendrimer encapsulation enhances anti-inflammatory efficacy of silver nanoparticles. Journal of Pediatric Surgery, 49(12), 1846-1851. https://doi.org/10.1016/j.jpedsurg.2014.09.033

[39] Mani, M., Okla, M. K., Selvaraj, S., Ram Kumar, A., Kumaresan, S., Muthukumaran, A., Kaviyarasu, K., El-Tayeb, M. A., Elbadawi, Y. B., Almaary, K. S., Almunqedhi, B. M. A., & Elshikh, M. S. (2021). A novel biogenic Allium cepa leaf mediated silver nanoparticles for antimicrobial, antioxidant, and anticancer effects on MCF-7 cell line. Environmental Research, 198, 111199. https://doi.org/10.1016/j.envres.2021.111199

[40] McQuillan, J. S., Infante, H. G., Stokes, E., & Shaw, A. M. (2012). Silver nanoparticle enhanced silver ion stress response in *Escherichia coli* K12. Nanotoxicology, 6, 857-866. https://doi.org/10.3109/17435390.2011.626532

[41] Mohamed, A. F., Nasr, M., Amer, M. E., Abuamara, T. M. M., Abd-Elhay, W. M., Kaabo, H. F., Matar, E. E. R., El Moselhy, L. E., Gomah, T. A., Deban, M. A. E.-F., & Shebl, R. I. (2022). Anticancer and antibacterial potentials induced post short-term exposure to electromagnetic field and silver nanoparticles and related pathological and genetic alterations: In vitro study. Infectious Agents and Cancer, 17(1), 4. https://doi.org/10.1186/s13027-022-00416-4

[42] Mosmann, T. (1983). Rapid colorimetric assay for cellular growth and survival: Application to proliferation and cytotoxicity assays. Journal of Immunological Methods, 65(1-2), 55-63. https://doi.org/10.1016/0022-1759(83)90303-4

[43] Nguyen, M. P., Pham, D. P., & Kim, D. (2022). Oxidative stress-induced silver nano-carriers for chemotherapy. Pharmaceuticals, 15(12), 1449. https://doi.org/10.3390/ph15121449

[44] Oufir, M., Seiler, C., Gerodetti, M., Gerber, J., Fürer, K., Mennet-von Eiff, M., Elsas, S.-M., Brenneisen, R., von Mandach, U., Hamburger, M., & Potterat, O. (2015). Quantification of bufadienolides in *Bryophyllum pinnatum* leaves and

manufactured products by UHPLC-ESIMS/MS. Planta Medica, 81(12-13), 1190-1197. https://doi.org/10.1055/s-0035-1546126

[45] Patil, M. P., & Kim, G.-D. (2017). Eco-friendly approach for nanoparticles synthesis and mechanism behind antibacterial activity of silver and anticancer activity of gold nanoparticles. Applied Microbiology and Biotechnology, 101(1), 79-92. https://doi.org/10.1007/s00253-016-8012-8

[46] Raja, G., Jang, Y.-K., Suh, J.-S., Kim, H.-S., Ahn, S. H., & Kim, T.-J. (2020). Microcellular environmental regulation of silver nanoparticles in cancer therapy: A critical review. Cancers, 12(3), 664. https://doi.org/10.3390/cancers12030664

[47] Ren, G., Hao, X., Yan, S., Chen, J., Qiu, G., Ang, K. P., & Tamrin, M. I. M. (2022). Abies spectabilis-mediated silver nanoparticles inhibits cell growth and promotes apoptosis in breast cancer MCF-7 cells. Journal of Environmental Pathology, Toxicology and Oncology, 41(1), 73-83. https://doi.org/10.1615/JEnvironPatholToxicolOncol.2021039805

[48] Rivera, M. D., Vázquez-Duhalt, R., Castro-Longoria, E., & Juárez-Moreno, K. (2024). Synergistic anticancer effects and reduced genotoxicity of silver nanoparticles and tamoxifen in breast cancer cells. Journal of Biochemical and Molecular Toxicology, 38(10), e23823. https://doi.org/10.1002/jbt.23823

[49] Sankar, R., Karthik, A., Prabu, A., Karthik, S., Shivashangari, K. S., & Ravikumar, V. (2013). Origanum vulgare mediated biosynthesis of silver nanoparticles for its antibacterial and anticancer activity. Colloids and Surfaces B: Biointerfaces, 108, 80-84. https://doi.org/10.1016/j.colsurfb.2013.02.033

[50] Santos, S., Haslinger, C., Klaic, K., Faleschini, M. T., Mennet, M., Potterat, O., von Mandach, U., Hamburger, M., & Simões-Wüst, A. P. (2019). A bufadienolide-enriched fraction of *Bryophyllum pinnatum* inhibits human myometrial contractility *in vitro*. Planta Medica, 85(5), 385-393. https://doi.org/10.1055/a-0810-7704

[51] Santos, S., Zurfluh, L., Mennet, M., Potterat, O., von Mandach, U., Hamburger, M., & Simões-Wüst, A. P. (2021). *Bryophyllum pinnatum* compounds inhibit oxytocin-induced signaling pathways in human myometrial cells. Frontiers in Pharmacology, 12, 632986. https://doi.org/10.3389/fphar.2021.632986

[52] Saravanan, V., Murugan, S. S., & Kumaravel, T. S. (2020). Genotoxicity studies with an ethanolic extract of *Kalanchoe pinnata* leaves. Mutation Research/Genetic Toxicology and Environmental Mutagenesis, 856-857, 503229. https://doi.org/10.1016/j.mrgentox.2020.503229

[53] Sharma, G., Jangra, A., Sihag, S., Chaturvedi, S., Yadav, S., & Chhokar, V. (2024). *Bryophyllum pinnatum* (Lam.) Oken: Unravelling therapeutic potential and navigating toxicity. Physiology and Molecular Biology of Plants, 30(9), 1413-1427. https://doi.org/10.1007/s12298-024-01509-7

[54] Sharma, V. K., Yngard, R. A., & Lin, Y. (2009). Silver nanoparticles: Green synthesis and their antimicrobial activities. Advances in Colloid and Interface Science, 145(1-2), 83-96. https://doi.org/10.1016/j.cis.2008.09.002

[55] Silva, M. M., Santos, M. R., Caroço, G., Rocha, R., Justino, G., & Mira, L. (2002). Structure-antioxidant activity relationships of flavonoids: A re-examination. Free Radical Research, 36(11), 1219-1227. https://doi.org/10.1080/1071576021000016472

[56] Tetali, S. D., Acharya, S., Ankari, A. B., Nanakram, V., & Raghavendra, A. S. (2021). Metabolomics of Withania somnifera (L.) Dunal: Advances and applications. Journal of Ethnopharmacology, 267, 113469. https://doi.org/10.1016/j.jep.2020.113469

[57] Thomas, S., Gonsalves, R. A., Jose, J., Zyoud, S. H., Prasad, A. R., & Garvasis, J. (2024). Plant-based synthesis, characterization approaches, applications and toxicity of silver nanoparticles: A comprehensive review. Journal of Biotechnology, 394, 135-149. https://doi.org/10.1016/j.jbiotec.2024.08.009

[58] Torres Castañeda, H. G., Colmenares Dulcey, A. J., & Isaza Martínez, J. H. (2016). Flavonoid glycosides from Siparuna gigantotepala leaves and their antioxidant activity. Chemical and Pharmaceutical Bulletin, 64(5), 502-506. https://doi.org/10.1248/cpb.c15-00788

[59] Tournebize, J., Sapin-Minet, A., Bartosz, G., Leroy, P., & Boudier, A. (2013). Pitfalls of assays devoted to evaluation of oxidative stress induced by inorganic nanoparticles. Talanta, 116, 753-763. https://doi.org/10.1016/j.talanta.2013.07.077

[60] Vahabirad, M., Daei, S., Abbasalipourkabir, R., & Ziamajidi, N. (2024). Anticancer action of silver nanoparticles in SKBR3 breast cancer cells through promotion of oxidative stress and apoptosis. BioMed Research International, 2024, 7145339. https://doi.org/10.1155/2024/7145339

[61] Yang, X., Gondikas, A. P., Marinakos, S. M., Auffan, M., Liu, J., Hsu-Kim, H., & Meyer, J. N. (2012). Mechanism of silver nanoparticle toxicity is dependent on dissolved silver and surface coating in Caenorhabditis elegans. Environmental Science & Technology, 46(2), 1119-1127. https://doi.org/10.1021/es202417t

[62] Yilma, A. N., Singh, S. R., Dixit, S., & Dennis, V. A. (2013). Anti-inflammatory effects of silver-polyvinyl pyrrolidone (Ag-PVP) nanoparticles in mouse macrophages infected with live Chlamydia trachomatis. International Journal of Nanomedicine, 8, 2421-2432. https://doi.org/10.2147/IJN.S44090

[63] Zhang, L., & Wang, W.-X. (2023). Silver nanoparticle toxicity to the larvae of oyster Crassostrea angulata: Contribution of *in vivo* dissolution. Science of the Total Environment, 858(Pt 2), 159965. https://doi.org/10.1016/j.scitotenv.2022.159965